



Unveiling the remarkable $deNO_x$ performance of $MnMoVO_x$ catalysts via dual regulation of the redox and acid sites

Yonglong Li^a, Guobo Li^a, Yu Zou^a, Wenming Liu^b, Hongxiang Zhang^a, Shengyong Lu^c, Zhenguo Li^d, Shule Zhang^e, Honggen Peng^{a,b,*}

^a School of Resources and Environment, Nanchang University, 999 Xuefu Road, Nanchang, Jiangxi 330031, PR China

^b School of Chemistry and Chemical Engineering, Nanchang University, 999 Xuefu Road, Nanchang, Jiangxi 330031, PR China

^c State Key Laboratory for Clean Energy Utilization, Institute for Thermal Power Engineering, Zhejiang University, Hangzhou 310027, PR China

^d National Engineering Laboratory for Mobile Source Emission Control Technology, China Automotive Technology & Research Center, Tianjin 300300, PR China

^e School of Chemical Engineering, Nanjing University of Science and Technology, Nanjing 210094, PR China

ARTICLE INFO

Keywords:

NO_x removal

NH_3 -SCR

Dual active sites regulation strategy

$MnMoVO_x$ catalyst

Alkali resistance

ABSTRACT

Developing NH_3 -SCR catalysts possessing excellent NO conversion, N_2 selectivity, and alkali-tolerance at low-temperatures remains a great challenge. MnO_x -based catalysts have attracted attention due to their exceptional low-temperature NH_3 -SCR activity. However, their strong oxidative capabilities often lead to excessive NH_3 oxidation, causing a narrow operating temperature window and low N_2 selectivity. In this study, we employed Mo and V to simultaneously fine-tune the acid and redox sites of MnO_x , effectively suppressing the excessive NH_3 oxidation at medium-high temperatures. The adjusted $Mn_{0.90}Mo_{0.09}V_{0.01}O_x$ catalyst demonstrated excellent low-temperature activity, a significantly broader active temperature window, and robust resistance to alkali metal poisoning. Multiple characterization results indicate that this dual acid-redox sites regulation strategy appropriately weakens the oxidative capacity while notably enhances surface acidity of the catalyst. Furthermore, the combination of in situ DRIFTS and DFT calculations reveal that following the adjustments of Mo and V on MnO_x , new Brønsted acid sites are generated. Besides, the regulated catalyst evidently inhibits NO adsorption and nitrate species formation, thus promoting the reaction exclusively through the E-R mechanism, resulting in boosted N_2 selectivity. This study also demonstrates that the optimum NH_3 -SCR performance of catalyst is achieved when oxidation ability and acid sites are harmoniously balanced, rather than following a "stronger is better" trend. In addition, through effective dual-active site regulation, the K-poisoning catalyst retains satisfactory catalytic activity. Thereby, the proposed dual-active sites regulation strategy in this study offers beneficial insights for the development of high-performance denitration catalysts.

1. Introduction

Controlling NO_x ($x = 1, 2$) emissions is a critical issue for an industrial chemical process that depends on thermal energy generated by the combustion of fossil fuels [1–4]. For stationary resources like coal-fired power plants and waste treatment plants, selective catalytic reduction with NH_3 (NH_3 -SCR) has become the predominant method for transforming harmful NO_x into benign N_2 and H_2O . Commercial V_2O_5 - WO_3 (MoO_3)/ TiO_2 catalysts have long been used as industrial catalysts for stationary resources owing to their high denitration ($deNO_x$) performance and tolerance to SO_2 poisoning [5,6]. Nevertheless, the catalysts still exhibit certain limitations, including a narrow

operating temperature window (300–400 °C), and non-selective oxidation of NH_3 to N_2O at high temperature [1,7]. Moreover, in most cases, the temperature of exhaust smoke NO_x emitted from stationary resources is lower than 300 °C, rendering traditional supported vanadium/titanium-based catalysts inadequate for NO_x elimination [8–11]. On the other hand, the SCR process invariably encounters various contaminants, such as alkali metals, within the intricate flue gas composition, leading to reduced catalytic activity and a shortened lifespan [12,13]. Hence, it is imperative to develop NH_3 -SCR catalysts offering superior low-temperature activity, high N_2 selectivity, satisfactory resistance to alkali metal, and an extended operational temperature range as feasible alternatives.

* Corresponding author at: School of Resources and Environment, Nanchang University, 999 Xuefu Road, Nanchang, Jiangxi 330031, PR China.

E-mail address: penghonggen@ncu.edu.cn (H. Peng).

<https://doi.org/10.1016/j.apcatb.2023.123612>

Received 15 October 2023; Received in revised form 19 November 2023; Accepted 30 November 2023

Available online 18 December 2023

0926-3373/© 2023 Elsevier B.V. All rights reserved.

It was widely accepted that both acid sites and redox sites are two crucial factors in the development of outstanding SCR catalysts. These sites play a dual role, influencing the adsorption/activation of NH_3 and NO_x , thus promoting the reaction pathways leading to the production of N_2 and H_2O [1,14]. The remarkable catalytic activity of the catalyst is attributed to the synergistic interaction between these two active sites, which do not work in isolation. Different oxide catalysts may exhibit varying redox and acidic characteristics, potentially producing important active intermediates that facilitate the SCR reaction. During the NH_3 -SCR reaction processes, both redox and acidic sites are indispensable. In general, the low-temperature activity of catalysts is governed by their redox properties, while surface acidity tends to dictate high-temperature activity [15]. Exceptional redox capability can generate active NH_2 and NO_2 species, thereby enhancing reaction efficiency via the Eley-Rideal (E-R) mechanism and "fast SCR", respectively [1]. Strong acidity supports the formation of adsorbed $\text{NH}_3/\text{NH}_4^+$ species, which are essential for the production of NH_2 species or their subsequent interactions with active nitrites or nitrates [1]. Over the decades, great efforts have been dedicated to boosting the NH_3 -SCR performance by regulating the redox properties or acid properties of the catalysts. Zhu et al. [16] found that proper amount of W doping can notably enhance the abundance of Brønsted and Lewis acid sites, contributing to the high-performance of $\text{Cu}_{0.02}\text{Fe}_{0.2}\text{W}_{0.02}\text{TiO}_x$ catalysts. Some other metal oxide catalysts such as $\text{V}_2\text{O}_5/\text{SnTiO}_2$ [17], $\text{Cu}_x\text{-Nb}_{1.1-x}$ [18], Fe-W [19], and Dy-MnFeO_x [20] also promoted the oxidation of NO to NO_2 due to their excellent redox properties. Despite this, only a limited number of researchers have achieved the creation of catalysts with exceptional catalytic performance and satisfactory resistance to alkali poisoning by simultaneously fine-tuning both redox and acid sites.

Because of their varying valence states and strong redox abilities, MnO_x -based catalysts typically exhibit excellent NH_3 -SCR activity at low temperature [21,22]. However, pure MnO_x catalysts suffer from a narrow operating temperature window and low N_2 selectivity at high temperatures, limiting their practical applications [23–25]. In order to improve the catalytic performance of MnO_x catalysts, extensive researches have been dedicated to modifying or doping them with additional transition or rare earth metal oxides to tune their redox or acidic properties [26,27]. For example, Dong et al. [28] found that TiO_2 modification effectively restrains the strong interaction between MnO_x species and the CeO_2 -ZrO₂ nanorod support, thus weakening the redox properties of. This advantageous modification suppressed the non-selective catalytic oxidation of NH_3 to N_2O , which led to a significant improvement in N_2 selectivity. In another study, Shan et al. [29] reported that the addition of W expanded the active temperature window of $\text{Mn}_{0.5}\text{TiO}_x$. It was demonstrated that the introduction of W reduced the capacity for NO/ NH_3 oxidation while generating more Brønsted and Lewis acid sites, both of which enhanced SCR activity at high temperatures. Therefore, achieving a balanced and fine-tuned combination of these acid and redox active sites is crucial for optimal catalytic performance.

In this work, Mo and V were utilized to simultaneously regulate the acid and redox sites of the MnO_x catalyst. The tuned ternary $\text{Mn}_{0.90}\text{Mo}_{0.09}\text{V}_{0.01}\text{O}_x$ catalyst displayed remarkable low-temperature NH_3 -SCR activity, much wider active temperature range, and higher N_2 selectivity compared to pure MnO_x catalyst. Meanwhile, the optimal catalyst also showed satisfactory tolerance to alkali metal. This study comprehensively explores the effects of Mo and V tuning, as well as the impact of K-poisoning on the redox and acidic properties of the catalysts, establishing deep connections between these chemical properties and catalytic activity. The outcomes in this study may pave the way for a feasible method to design high-efficiency *deNO_x* catalysts through the dual regulation of redox and acid sites.

2. Experimental section

2.1. Preparation of catalysts

The $\text{Mn}(\text{NO}_3)_2$ (50 wt%) solution were purchased from Aladdin Co. Ltd., concentrated hydrochloric acid (36.0 – 38.0%), $(\text{NH}_4)_6\text{Mo}_7\text{O}_{24}\cdot 4\text{H}_2\text{O}$ (98.5%) and ammonia solution (25 wt%) were purchased from Xilong Scientific Co. Ltd, and NH_4VO_3 (99%) was purchased from Adamas-beta Co. Ltd. All chemicals were used without further purification.

Fresh $\text{Mn}_{0.90}\text{Mo}_\delta\text{V}_{0.10-\delta}\text{O}_x$ ($\delta = 0, 0.01, 0.03, 0.05, 0.07, 0.09$) catalysts with varying Mo/V ratios were synthesized using the co-precipitation method. Typically, moderate NH_4VO_3 was first dissolved in distilled water (70 °C) and stirred for 15 min (denoted as A solution). After the temperature of A solution decreased to room temperature, 53.4703 g of $\text{Mn}(\text{NO}_3)_2$ solution was added into A solution slowly (denoted as B solution). Following 10 min of stirring, appropriate amounts of $(\text{NH}_4)_6\text{Mo}_7\text{O}_{24}\cdot 4\text{H}_2\text{O}$ was dissolved in B (denoted as C solution). After an additional 10 min of stirring, 10 mL concentrated hydrochloric acid and distilled water were added in turn till the total metal ion concentration was 0.415 mol L^{-1} (denoted as D solution). After 3 h of stirring, diluted ammonia solution was slowly added to the above mixed solution under vigorous stirring until the pH was approximately 10. After stirring for 3 h, then the obtained suspension was filtered and washed with deionized water and ethanol several times. Finally, the precipitate was dried at 80 °C for 12 h and subsequently calcined at 550 °C for 5 h in air (5°C min^{-1} heating rate). Afterwards, the desired $\text{Mn}_{0.90}\text{Mo}_\delta\text{V}_{0.10-\delta}\text{O}_x$ catalysts with different Mo and V content were obtained, and the molar ratio of Mn: Mo: V was fixed at 0.90: δ : 0.10 – δ ($\delta = 0.01, 0.03, 0.05, 0.07, 0.09$). For comparison, MnO_x , $\text{Mn}_{0.90}\text{Mo}_{0.10}\text{O}_x$ and $\text{Mn}_{0.90}\text{V}_{0.10}\text{O}_x$ samples were also prepared by the same procedures without NH_4VO_3 and/or $(\text{NH}_4)_6\text{Mo}_7\text{O}_{24}\cdot 4\text{H}_2\text{O}$ addition, respectively. Before SCR activity tests, the fresh catalysts were pressed, crushed, and sieved to 40 – 60 mesh.

Afterward, potassium was deposited by wet impregnation with a solution of potassium nitrate to get K-poisoning samples. Typically, the obtained fresh sample was added into the KNO_3 aqueous solution under vigorous stirring at room temperature for 30 min. Then the mixture was dried and calcined at 500 °C for 2 h in air. The K_2O loading was 0.5 wt%. The poisoned samples were named as $\text{MnO}_x\text{-K}$, $\text{Mn}_{0.90}\text{Mo}_{0.10}\text{O}_x\text{-K}$, $\text{Mn}_{0.90}\text{V}_{0.10}\text{O}_x\text{-K}$ and $\text{Mn}_{0.90}\text{Mo}_\delta\text{V}_{0.10-\delta}\text{O}_x\text{-K}$ ($\delta = 0.01, 0.03, 0.05, 0.07, 0.09$), respectively. Before SCR activity tests, the poisoned catalysts were also pressed, crushed, and sieved to 40 – 60 mesh.

2.2. Catalyst characterizations

Powder X-ray diffraction (XRD) measurements in the 2θ range of 10–90° were obtained using a Rigaku SmartLab 9KW X-ray diffractometer (Rigaku Corporation, Tokyo, Japan) with $\text{Cu K}\alpha$ radiation. The BET surface areas of the catalysts were determined from nitrogen adsorption/desorption isotherms by a Kubo-X1000 specific surface area analyzer. Prior to the measurement, the sample was degassed in vacuum at 300 °C for 5 h to remove adsorbed water. The H_2 temperature-programmed reduction (H_2 -TPR) experiments were conducted on a PCA-1200 (Builder, Beijing) instrument. Typically, 100 mg of catalyst was pretreated under a pure He atmosphere at 300 °C for 1.5 h and then cooled down to room temperature. Finally, the sample was heated to 1000 °C in a 10% H_2/Ar under a flow rate of 30 mL min^{-1} at a heating rate of $10^\circ\text{C min}^{-1}$.

Scanning electron microscope (SEM) was carried out on the FEI Nova NanoSEM450 in a high vacuum mode and a high voltage of 15.00 kV with an OXFORD N50 detector. The transmission electron microscopy (TEM) images were obtained from a JEM-2100 instrument. The energy dispersive spectroscopy (EDS) elemental mapping images were collected on from a JEOL 2800 instrument equipped with a dual-type EDS detector. X-ray photoelectron spectroscopy (XPS) was performed on an

Escalab 250Xi spectrometer (Thermo, USA) equipped with Al K α radiation (1486.6 eV), and binding energies (BE) of all the elements were calibrated with C1s at 284.8 eV. The Raman spectra were measured on a Renishaw inVia Raman microscope with a 532 nm visible laser source. Temperature-programmed desorption of NH₃ (NH₃-TPD) was measured via an automatic chemical adsorption instrument (BelCAT-II, Japan) equipped with both TCD and mass detectors (BelMass, Japan) to monitor the NH₃. Prior to the NH₃-TPD experiments, 100 mg catalyst was outgassed under He protection (30 mL min⁻¹) at 300 °C for 1 h and then cooled to 50 °C. Then, the sample was exposed to 10% NH₃/He for 1 h at 50 °C, the physical adsorption of ammonia was removed by He purging for 1 h at the same temperature. Finally, the temperature was raised to 800 °C with a ramping rate of 10 °C min⁻¹.

The in situ diffuse reflectance infrared Fourier transform spectroscopy (in situ DRIFTS) measurements were performed on an FTIR (Thermo Scientific Nicolet IS50) equipped with a Harrick DRIFTS cell and a mercury-cadmium-telluride (MCT) detector cooled by liquid nitrogen. The NH₃, NO + O₂ adsorption and transient DRIFT spectra were collected in the range of 1000 – 4000 cm⁻¹ in Kubelka-Munk format, accumulating 64 scans at 4 cm⁻¹ resolution. Before each test, the samples were pretreated at 400 °C in a N₂ flow (50 mL min⁻¹) for 1.5 h and cooled to target temperature under N₂ flow. The background spectrum at the desired temperature was collected after pretreatment under N₂ atmosphere, which would be deduced from the sample spectra for each measurement. The reaction conditions were controlled as follows: 50 mL min⁻¹ total flow rate, 1000 ppm NH₃, 1000 ppm NO + 5 vol% O₂ and N₂ balance. For each sample, the NH₃ or (NO + O₂) adsorption time was controlled at 50 or 60 min. Afterwards, the samples were purged by N₂ for another 30 min until the infrared spectroscopy signals were stabilized. Finally, (NO + O₂)/NH₃ was introduced into the gas chamber to react with the pre-adsorbed NH₃/NO_x.

2.3. Catalytic activity tests

NH₃-SCR activity measurements were conducted using a fixed-bed quartz reactor with an inner diameter of 6 mm, containing catalyst particles ranging from 40 to 60 mesh sizes. The gas composition consisted of 500 ppm of NO, 500 ppm of NH₃, 5 vol% O₂, and N₂ as the balance gas, with a total flow rate of 100 mL min⁻¹. This configuration resulted in a weight hourly space velocity (WHSV) of 60,000 mL g_{cat}⁻¹ h⁻¹. Before each activity measurement, 100 mg of catalyst underwent a one-hour sweep with a flow of 100 mL min⁻¹ N₂ at 300 °C to eliminate physisorbed H₂O. Subsequently, the background infrared (IR) spectrum of the reactor effluent was recorded in a nitrogen atmosphere at room temperature. Following this, the IR spectra of the simulated feed effluent from the reactor were recorded for 1 h to ensure a uniform mixture. The catalytic activity performance measurements involved heating the fixed-bed at a rate of 2 °C min⁻¹. The composition and concentration of the outlet gas were continuously analyzed by Fourier transform infrared (FT-IR) spectroscopy using a Antaris IGS-Gas Analyzer (Thermo Fisher Scientific Inc., Waltham, MA, USA) equipped with a 2-meter gas cell. NO_x conversion and N₂ selectivity were then calculated using the following equations:

$$X_{\text{NO}_x} = \left(1 - \frac{[\text{NO}_x]_{\text{outlet}}}{[\text{NO}_x]_{\text{inlet}}}\right) \times 100\% \quad (1)$$

$$S_{\text{N}_2} = \left(1 - \frac{2[\text{N}_2\text{O}]_{\text{outlet}}}{[\text{NO}_x]_{\text{inlet}} - [\text{NO}_x]_{\text{outlet}} + [\text{NH}_3]_{\text{inlet}} - [\text{NH}_3]_{\text{outlet}}}\right) \times 100\% \quad (2)$$

In these equations, X_{NO_x} represents the NO_x at a certain temperature (%), where $[\text{NO}_x] = [\text{NO}] + [\text{NO}_2]$, $[\text{NO}_x]_{\text{inlet}}$ and $[\text{NO}_x]_{\text{outlet}}$ are the inlet and outlet gas NO_x concentrations, respectively. $[\text{NH}_3]_{\text{inlet}}$ and $[\text{NH}_3]_{\text{outlet}}$ are the inlet and outlet gas NH₃ concentrations, respectively. Lastly, $[\text{N}_2\text{O}]_{\text{outlet}}$ is the concentration of N₂O in the outlet gas.

The catalytic oxidation of NO to NO₂ was also measured under the

same conditions above except for the absence of NH₃. The conversion percentage of NO to NO₂ in the oxidation reaction was calculated using the following equation:

$$X_{\text{NO} \rightarrow \text{NO}_2} = \frac{[\text{NO}_2]_{\text{outlet}}}{[\text{NO}]_{\text{inlet}}} \times 100\% \quad (3)$$

Similarly, the catalytic oxidation of NH₃ was also measured under the same conditions except for the absence of NO. The NH₃ conversion percentage in oxidation reaction was calculated as follows:

$$X_{\text{NH}_3} = \left(1 - \frac{[\text{NH}_3]_{\text{outlet}}}{[\text{NH}_3]_{\text{inlet}}}\right) \times 100\% \quad (4)$$

2.4. Kinetics tests

In the investigation of NH₃-SCR kinetics over Mn_{0.90}Mo_{0.10}-δO_x (δ = 0.01, 0.03, 0.05, 0.07, 0.09) catalysts, a fixed-bed quartz reactor was employed. Within a quartz tube of 6 mm inner diameter, 25 mg of catalyst and 75 mg of inert quartz sand (40–60 mesh) were packed. Although maintaining the same composition and concentration of reaction gases as NH₃-SCR, the total flow rate was adjusted to 350 mL min⁻¹, thereby fixing the WHSV at 840,000 mL g_{cat}⁻¹ h⁻¹ and ensuring NO_x conversion rates remained below 15%. The low NO_x conversion and the absence of mass and heat transfer limitations confirm the occurrence of the reaction in the kinetic region. To further corroborate this, calculations of the Weisz-Prater criterion and the Mears criterion were undertaken [30–32], systematically excluding the influences of mass transport and heat transfer limitations, respectively. The determination of reaction rate (r , in mol g_{cat}⁻¹ s⁻¹), reaction rate coefficient (k , in mol g_{cat}⁻¹ s⁻¹) and apparent activation energy (E_a , in kJ mol⁻¹) for the NH₃-SCR kinetic reactions involves conducting experiments at varying temperatures to derive the NO_x conversion using the following formulas:

$$r = \frac{X_{\text{NO}_x} F_{\text{NO}_x}}{m_{\text{cat}}} \quad (5)$$

$$k = -\frac{F_{\text{NO}_x}}{m_{\text{cat}}} \times \ln(1 - X_{\text{NO}_x}) \quad (6)$$

$$\ln k = -\frac{E_a}{RT} + \ln A \quad (7)$$

Here, F_{NO_x} represents the gas flow rate (in mol s⁻¹) of NO_x, m_{cat} is the mass of the catalyst (in g), A is the pre-exponential factor, T is the reaction temperature (in K), R is the gas constant (in kJ mol⁻¹ K⁻¹). The reaction orders for NO and NH₃ are typically set as first and zero, respectively, and the E_a can be calculated from the Arrhenius plots of the reaction rate coefficient.

2.5. Density functional theory (DFT) calculation

The Vienna Ab initio Simulation Package (VASP) is adopted for the DFT calculations [33]. The projector augmented wave (PAW) method is used to solve the Kohn-Sham equations [34]. The generalized gradient approximation and Perdew-Burke-Ernzerhof (GGA-PBE) exchange association functional is adopted [35]. A Hubbard-like term (U_{eff}) was added to the PBE functional (DFT + U_{eff}) employing the rotationally invariant formalism [36], in which U_{eff} value was 3.0 eV for Mn [37], U_{eff} value was 2.0 eV for V [38]. Specific parameter settings and slab model information are shown in the Supporting Information.

3. Results and discussion

3.1. NH₃-SCR Performance over the MnCoVO_x catalysts

The NO_x conversion and N₂ selectivity as a function of temperature

for NH_3 -SCR over the catalysts are displayed Fig. 1 (A) and (B), respectively. The pure MnO_x catalyst exhibits commendable low-temperature activity, achieving a 96% NO_x conversion at 200 °C. However, MnO_x has a relatively narrow active temperature window, with a sharp decline in activity above 225 °C and near inactivation at 400 °C. Furthermore, the N_2 selectivity over the MnO_x catalyst is unsatisfactory, significant N_2O by-products are generated during the NH_3 -SCR processes due to the undesirable over-oxidation of NH_3 (Fig. S1). Throughout the temperature range, the selectivity for N_2 shows a declining trend, falling below 80% between 300 – 500 °C. Surprisingly, the low-temperature activity, especially the operating temperature window and N_2 selectivity improves after Mo modification the on MnO_x . The $\text{Mn}_{0.90}\text{Mo}_{0.10}\text{O}_x$ catalyst achieves over 80% NO_x conversion in the temperature range of approximately 183 – 351 °C, with N_2 selectivity above 80% when the temperature is below 450 °C. Nevertheless, the addition of V into MnO_x is not favor for low-temperature activity, as the $\text{Mn}_{0.90}\text{V}_{0.10}\text{O}_x$ catalyst exhibits lower activity than MnO_x at temperatures below 200 °C. Despite this, the activity at medium and high temperatures remarkably improves after V tuning, along with enhanced N_2 selectivity. It achieves over 80% NO_x conversion between approximately 190 – 432 °C and nearly 100% NO_x conversion at 225 – 375 °C. $\text{Mn}_{0.90}\text{V}_{0.10}\text{O}_x$ also displays excellent N_2 selectivity, with values consistently above 85% throughout the temperature range of 100 – 500 °C and even higher than 95% at 100 – 400 °C, with less than 50 ppm generated across the entire temperature range. In summary, V doping into MnO_x significantly expands the operational temperature range while enhancing N_2 selectivity. When considering the ternary $\text{Mn}_{0.90}\text{Mo}_\delta\text{V}_{0.10-\delta}\text{O}_x$ ($\delta = 0.01, 0.03, 0.05, 0.07, 0.09$) catalysts, further

enhancements in low-temperature activity and N_2 selectivity are observed compared to the binary $\text{Mn}_{0.90}\text{Mo}_{0.10}\text{O}_x$ catalyst. All five MnMoVO_x catalysts exhibit a wide working temperature window and remarkable N_2 selectivity. Among these catalysts, the $\text{Mn}_{0.90}\text{Mo}_{0.09}\text{V}_{0.01}\text{O}_x$ demonstrates the best NH_3 -SCR performance, achieving over 80% NO_x conversion across a broad temperature range from approximately 155 – 430 °C, with nearly 100% NO_x conversion between 200 – 375 °C. Furthermore, the N_2 selectivity remains consistently above 85% within the temperature range of 100 – 500 °C. Though Mo doping into MnO_x enhances low-temperature NH_3 -SCR activity, the operational temperature window of $\text{Mn}_{0.90}\text{Mo}_{0.10}\text{O}_x$ remains relatively narrow, and N_2 selectivity remains unsatisfactory. Conversely, V doping into MnO_x reduces low-temperature NH_3 -SCR activity but significantly widens the operational temperature window and enhances N_2 selectivity. These findings underscore the synergistic benefits of Mo and V co-regulation on MnO_x , which promote low-temperature NH_3 -SCR activity, broaden the operational temperature range, and improve N_2 selectivity. Importantly, the Mo/V ratios are shown to influence NH_3 -SCR activity.

To further assess the remarkable catalytic performance of the $\text{Mn}_{0.90}\text{Mo}_{0.09}\text{V}_{0.01}\text{O}_x$ catalyst and its counterparts, the reaction rate (r) and apparent activation energy (E_a) were calculated before excluding the mass and heat transfer limitations (see Supporting Information, Table S1 – S3). The SCR rate notably increases upon co-tuning the MnO_x catalyst with Mo and V, as evident in Fig. 1C. Moreover, as depicted in Fig. 1D, the SCR reaction over the pure MnO_x catalyst exhibits the highest apparent activation energy (48 kJ mol⁻¹). After V doped into MnO_x , the E_a experiences a slight reduction, resulting in 44 kJ mol⁻¹ for the $\text{Mn}_{0.90}\text{V}_{0.10}\text{O}_x$. Remarkably, the introduction of Mo

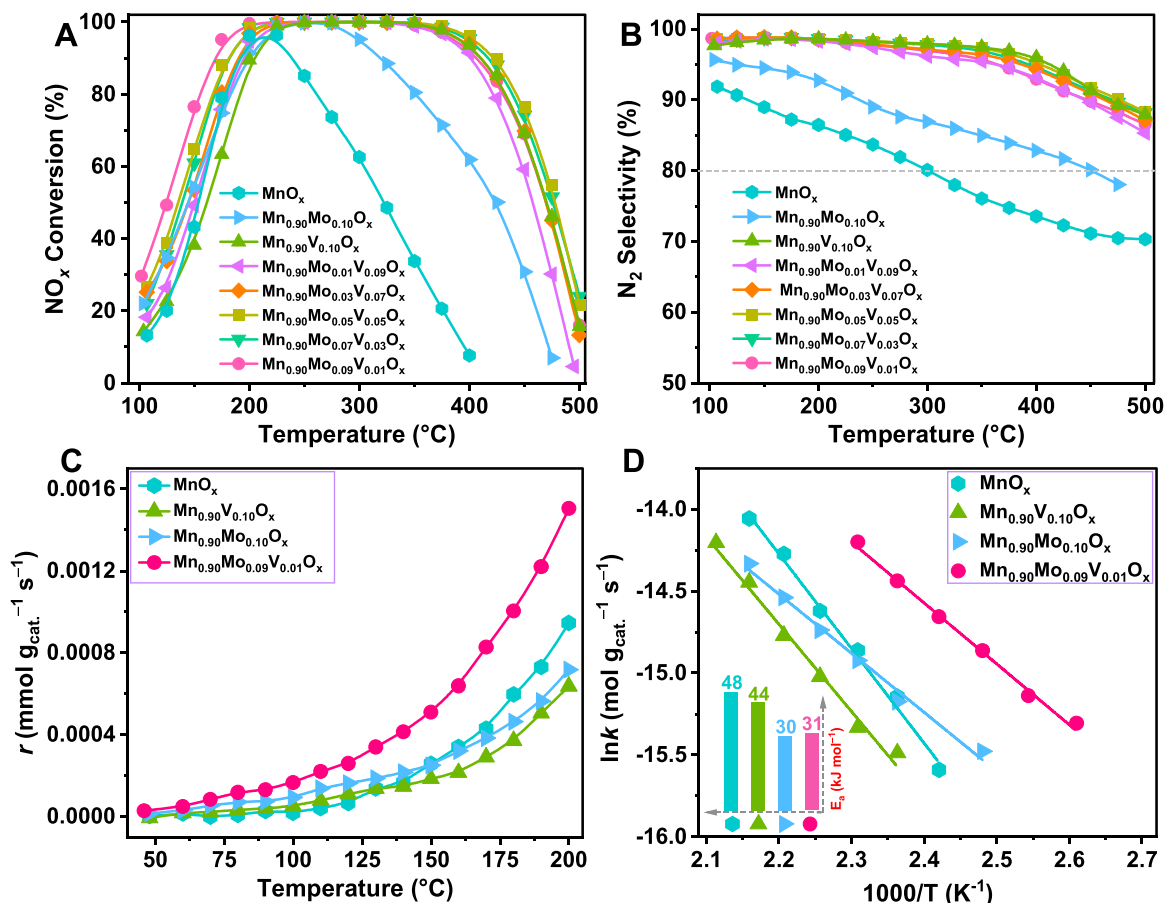


Fig. 1. Plots of (A) NO_x conversion and (B) N_2 selectivity as a function of reaction temperature over fresh MnO_x , $\text{Mn}_{0.90}\text{Mo}_{0.10}\text{O}_x$, $\text{Mn}_{0.90}\text{V}_{0.10}\text{O}_x$ and $\text{Mn}_{0.90}\text{Mo}_\delta\text{V}_{0.10-\delta}\text{O}_x$ ($\delta = 0.01, 0.03, 0.05, 0.07, 0.09$) catalysts. (C) Kinetic reaction rate r and (D) Arrhenius plots of NO_x conversions in SCR over the MnO_x , $\text{Mn}_{0.90}\text{V}_{0.10}\text{O}_x$, $\text{Mn}_{0.90}\text{Mo}_{0.10}\text{O}_x$ and $\text{Mn}_{0.90}\text{Mo}_{0.09}\text{V}_{0.01}\text{O}_x$ catalysts. Reaction conditions: (A, B) $[\text{NO}] = [\text{NH}_3] = 500$ ppm, $[\text{O}_2] = 5$ vol%, WHSV = 60,000 mL g_{cat}⁻¹ h⁻¹; (C, D) $[\text{NO}] = [\text{NH}_3] = 500$ ppm, $[\text{O}_2] = 5$ vol%, WHSV = 840,000 mL g_{cat}⁻¹ h⁻¹.

and Mo/V into MnO_x leads to a substantial decrease in E_a , with values of 30 and 31 kJ mol^{-1} for the $\text{Mn}_{0.90}\text{Mo}_{0.10}\text{O}_x$ and $\text{Mn}_{0.90}\text{Mo}_{0.09}\text{V}_{0.01}\text{O}_x$, respectively. These findings demonstrate that Mo and V co-tuning on MnO_x effectively reduces the energy barrier for the reaction, leading to a significant enhancement in the reaction rate. This observation aligns with the exceptional catalytic activity displayed by the $\text{Mn}_{0.90}\text{Mo}_{0.09}\text{V}_{0.01}\text{O}_x$ catalyst.

3.2. Alkali poisoning resistance of catalysts

The presence of alkali metals in fly ash poses a significant concern for SCR catalysts that employed in municipal solid waste incineration plants and coal-fired power plants, and these metals can somewhat diminish catalytic performance [39]. Hence, it becomes imperative to evaluate the alkali poisoning resistance of the catalysts. As illustrated in Fig. 2, the NH_3 -SCR activity after poisoned by K_2O are measured. In the case of the MnO_x -K catalyst (Fig. 2A), a surprising observation emerges: the low-temperature performance actually shows a slight improvement. At 150 $^\circ\text{C}$, the NO_x conversion increases from 43% to 50% upon K_2O deposition on MnO_x . This phenomenon could be attributed to alterations in the surface valence state composition of the MnO_x surface, thereby enhancing its oxidation capacity. A more detailed analysis of this is provided in the subsequent characterization results. However, as the temperature surpasses 160 $^\circ\text{C}$, a substantial decline in activity becomes evident. The highest achievable NO_x conversion over the MnO_x -K catalyst is merely 72% at 200 $^\circ\text{C}$, in stark contrast to the 96% conversion achieved with the fresh MnO_x catalyst. Furthermore, the MnO_x -K catalyst becomes entirely deactivated at a relatively low temperature of 350 $^\circ\text{C}$. Moving on to the $\text{Mn}_{0.90}\text{V}_{0.10}\text{O}_x$ -K catalyst (Fig. 2B), it exhibits minimal changes in activity at temperatures below 175 $^\circ\text{C}$ when compared to the fresh catalyst. However, a pronounced decrease in

activity, especially at medium and high temperatures, becomes apparent. The active temperature range notably narrowed, and the $\text{Mn}_{0.90}\text{V}_{0.10}\text{O}_x$ -K catalyst essentially loses its activity at 425 $^\circ\text{C}$, whereas the fresh $\text{Mn}_{0.90}\text{V}_{0.10}\text{O}_x$ catalyst maintains an 85% NO_x conversion rate. In contrast to the MnO_x -K and $\text{Mn}_{0.90}\text{V}_{0.10}\text{O}_x$ -K catalysts, the $\text{Mn}_{0.90}\text{Mo}_{0.10}\text{O}_x$ -K catalyst shows a clear reduction in low-temperature activity after K_2O poisoning (Fig. 2C). However, the decrease in high-temperature activity is comparatively milder when compared to the MnO_x -K and $\text{Mn}_{0.90}\text{V}_{0.10}\text{O}_x$ -K catalysts. This divergence can likely be attributed to the fact that $\text{Mn}_{0.90}\text{Mo}_{0.10}\text{O}_x$ possesses a higher concentration of strong acid sites, which can partially withstand the poisoning effect of K_2O . Numerous studies have affirmed that Mo doping can introduce additional acid sites that promote NH_3 -SCR performance [40, 41]. As depicted in Fig. 2D, although both the low-temperature activity and high-temperature activity have decreased over the $\text{Mn}_{0.90}\text{Mo}_{0.09}\text{V}_{0.01}\text{O}_x$ -K catalyst, the decline is relatively small, indicating excellent resistance to K_2O poisoning. After K_2O poisoning, the catalyst continues to exhibit strong low-temperature performance and maintains a broad operational temperature range. It achieves NO_x conversion rates exceeding 80% in the range of approximately 168 – 389 $^\circ\text{C}$, with NO_x conversion exceeding 90% in the range of approximately 184 – 369 $^\circ\text{C}$. Furthermore, N_2 selectivity over the $\text{Mn}_{0.90}\text{Mo}_{0.09}\text{V}_{0.01}\text{O}_x$ -K catalyst remains satisfactory, experiencing only a slight decrease. Above 82% N_2 selectivity can be maintained at temperatures ranging from 100 – 475 $^\circ\text{C}$. However, when examining other ternary $\text{Mn}_{0.90}\text{Mo}_\delta\text{V}_{0.10-\delta}\text{O}_x$ -K ($\delta = 0.01, 0.03, 0.05, 0.07$) catalysts (Fig. S2), it is evident that both low-temperature and high-temperature activities show a significant decline, accompanied by a noticeable decrease in N_2 selectivity. Generally, $\text{Mn}_{0.90}\text{Mo}_{0.09}\text{V}_{0.01}\text{O}_x$ exhibits the highest tolerance to K-poisoning, and also demonstrates superior NH_3 -SCR performance among all the poisoned catalysts (Fig. S3). Based on the K-resistance

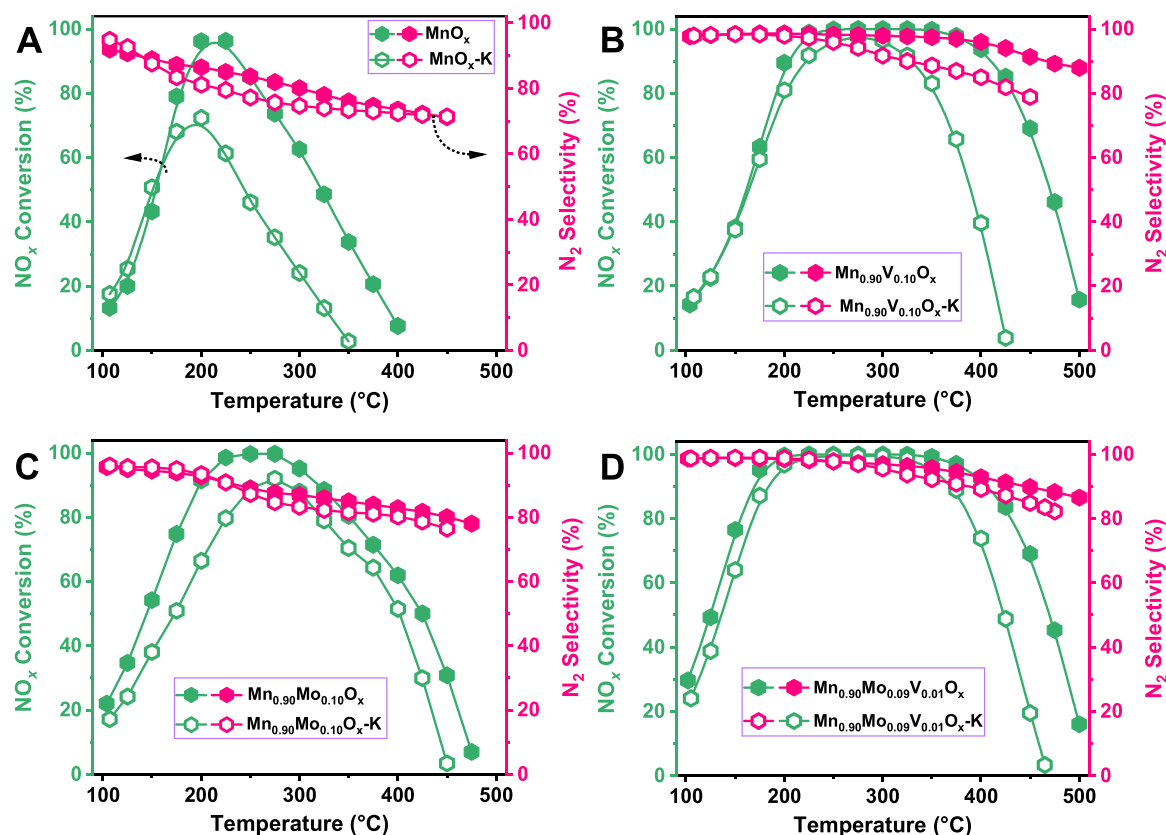


Fig. 2. Plots of NO_x conversion (green line) and N_2 selectivity (red line) as a function of reaction temperature over the fresh and poisoned MnO_x , $\text{Mn}_{0.90}\text{V}_{0.10}\text{O}_x$, $\text{Mn}_{0.90}\text{Mo}_{0.10}\text{O}_x$ and $\text{Mn}_{0.90}\text{Mo}_{0.09}\text{V}_{0.01}\text{O}_x$ catalysts. Reaction conditions: $[\text{NO}] = [\text{NH}_3] = 500$ ppm, $[\text{O}_2] = 5$ vol%, N_2 as a balance gas, and $\text{WHSV} = 60,000 \text{ mL g}_{\text{cat}}^{-1} \text{ h}^{-1}$.

performance of all the catalysts, it can be inferred that K_2O is detrimental to catalysts during NH_3 -SCR processes, resulting in a decrease in low-and/or high-temperature activity. On the other hand, co-tuning MnO_x with Mo and V in appropriate ratios markedly improves its resistance to K_2O poisoning.

3.3. Separated NH_3 and NO oxidation over the catalysts

In addition to the SCR reaction, the catalyst also facilitates the NH_3 oxidation process within a range of relatively high temperatures. This is considered a side reaction that can lead to the undesired formation of N_2O , NO, and NO_2 , as previously reported [1]. Excessive NH_3 oxidation is well-known as a major contributing factor to low NO_x conversion and reduced N_2 selectivity at high temperatures [42]. Thus, the catalytic activities on different fresh catalysts for the separate NH_3 oxidations are performed and shown in Fig. 3A. The light-off temperature with 50% conversion for NH_3 oxidation is 205 °C and total NH_3 conversion can be achieved at 375 °C on pure MnO_x . However, after Mo doping, NH_3 oxidation is notably suppressed in the $Mn_{0.90}Mo_{0.10}O_x$ sample, with the light-off temperature shifting to approximately 242 °C. Upon further addition of V, NH_3 oxidation exhibits less than 40% conversion at temperatures below 250 °C. For all ternary $Mn_{0.90}Mo_{0.10}V_{0.01-0.09}O_x$ ($\delta = 0.01, 0.03, 0.05, 0.07, 0.09$) catalysts, the complete NH_3 conversion is achieved above 425 °C. Among all the catalysts tested, pure MnO_x displays the highest NH_3 oxidation ability, followed by the ternary $Mn_{0.90}Mo_{0.10}V_{0.01-0.09}O_x$ ($\delta = 0.01, 0.03, 0.05, 0.07, 0.09$), whereas the binary $Mn_{0.90}V_{0.10}O_x$ sample exhibits the lowest capacity. It is generally

accepted that the NH_3 oxidation ability of catalysts is closely linked to their redox characteristics, implying that stronger oxidation properties are associated with higher NH_3 oxidation ability. Consequently, the results from separate NH_3 oxidation experiments indicate that Mo tuning, especially V tuning, effectively diminishes the oxidation ability of the MnO_x catalyst. Besides, Fig. S4 presents the selectivity of different products during separate NH_3 oxidation reactions over the fresh catalysts. The MnO_x catalyst exhibits the lowest N_2 selectivity (Fig. S4A). However, after co-tuning with Mo and V, the N_2 selectivity remarkably improves, this improvement is mainly attributed to the reduced production of N_2O and NO_2 (Fig. S4B, C). When combined with the above separate NH_3 oxidation results, we can conclude that the co-tuning of Mo and V on MnO_x effectively diminishes its oxidation ability, thus inhibiting unselective NH_3 oxidation processes. This inhibition is responsible for the enhanced activity and high N_2 selectivity at high temperatures observed over the ternary $Mn_{0.90}Mo_{0.10}V_{0.01-0.09}O_x$ ($\delta = 0.01, 0.03, 0.05, 0.07, 0.09$) catalysts. Separate NH_3 oxidation reactions over catalysts poisoned by K_2O were also conducted and are presented in Fig. 3B. Compared to the fresh MnO_x catalyst, MnO_x -K exhibits superior NH_3 oxidation ability, with a light-off temperature of only 165 °C, and nearly 100% NH_3 conversion achievable at 275 °C. In the case of $Mn_{0.90}Mo_{0.09}V_{0.01}O_x$ -K and $Mn_{0.90}Mo_{0.10}O_x$ -K catalysts, both show a decrease in NH_3 oxidation capacity. However, after K_2O poisoning, the decline in NH_3 oxidation ability over $Mn_{0.90}V_{0.10}O_x$ is negligible. Therefore, the results of separate NH_3 oxidation on the poisoned catalysts suggest that K_2O poisoning enhances the oxidation ability of the MnO_x catalyst, while the oxidation ability decreases over

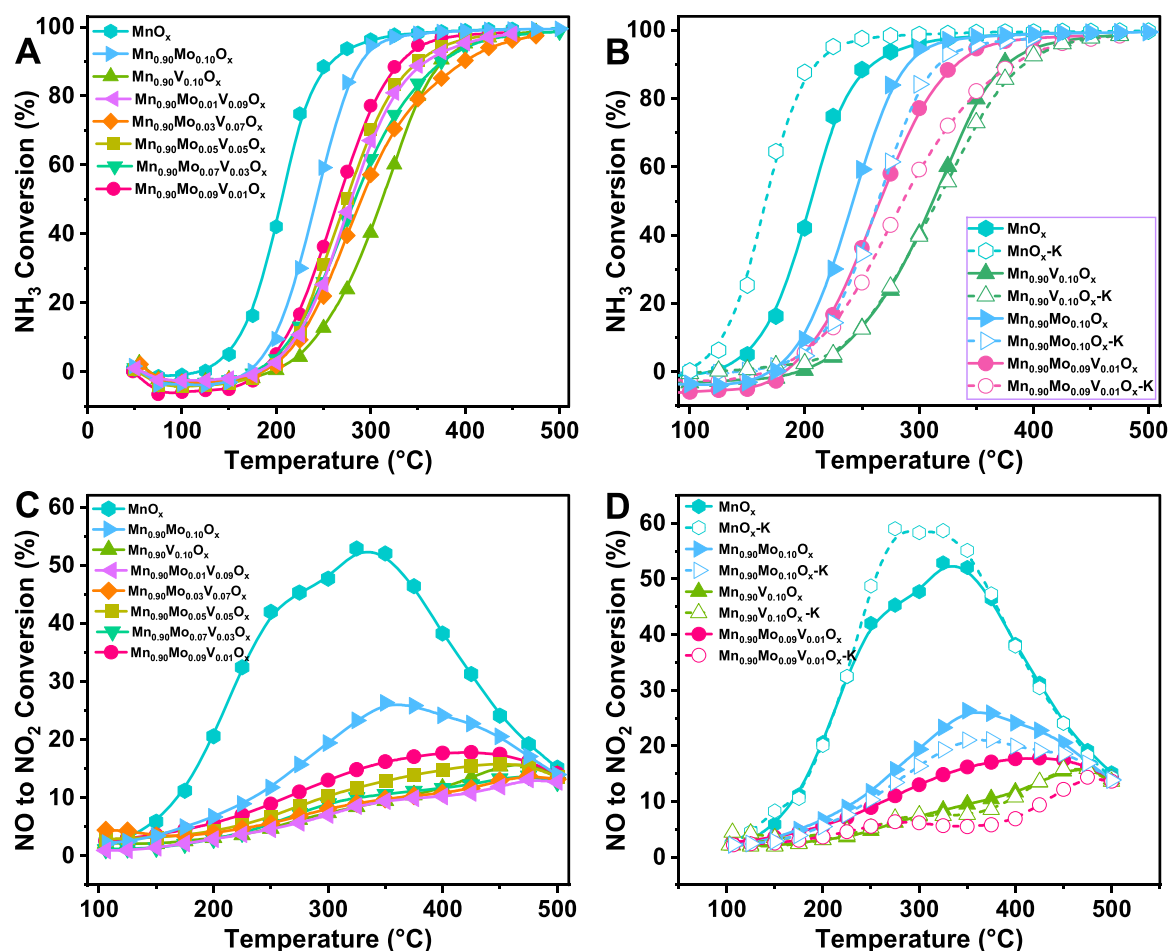


Fig. 3. (A, B) Plots of NH_3 conversion as a function of temperature over the fresh and poisoned catalysts when performing separate NH_3 oxidation reaction. Reaction conditions: $[NH_3] = 500$ ppm, $[O_2] = 5$ vol%, WHSV = 60,000 mL $g_{cat}^{-1} h^{-1}$. (C, D) Plots of NO conversion as a function of temperature over the fresh and poisoned catalysts when performing separate NO oxidation reaction. Reaction conditions: $[NO] = 500$ ppm, $[O_2] = 5$ vol%, WHSV = 60,000 mL $g_{cat}^{-1} h^{-1}$.

$\text{Mn}_{0.90}\text{Mo}_{0.10}\text{O}_x\text{-K}$ and $\text{Mn}_{0.90}\text{Mo}_{0.09}\text{V}_{0.01}\text{O}_x\text{-K}$ catalysts. Conversely, the oxidation ability remains almost unchanged over $\text{Mn}_{0.90}\text{V}_{0.10}\text{O}_x$. Similarly, Fig. S5 illustrates the selectivity of various products during separate NH_3 oxidation reactions over the poisoned catalysts, where all the N_2 selectivity over the poisoned catalysts decreases (Fig. S5A). Nonetheless, the reasons for the decline in selectivity differ between the two types of poisoned catalysts. For $\text{MnO}_x\text{-K}$ catalysts, the enhanced oxidation ability after poisoning further promotes the unselective oxidation of NH_3 , resulting in the formation of more NO_x rather than N_2O during NH_3 oxidation reactions (Fig. S5B, C) compared to fresh MnO_x . To confirm this, the concentrations of N_2O and NO_2 as a function of temperature during $\text{NH}_3\text{-SCR}$ reactions over both fresh and K-poisoned MnO_x catalysts are presented in Fig. S6. Though the N_2O concentrations are relatively similar, the NO_2 concentration over $\text{MnO}_x\text{-K}$ is significantly higher than that of fresh MnO_x . Therefore, the reduced N_2 selectivity in $\text{MnO}_x\text{-K}$ is primarily due to the increased production of NO_2 . After being deposited with K_2O , the oxidation capacity improves notably, and it is reasonable to assume that $\text{MnO}_x\text{-K}$ directly oxidizes NH_3 to NO_2 with a higher N valence. However, for other poisoned catalysts, apart from $\text{MnO}_x\text{-K}$, the decreased N_2 selectivity is mainly attributed to the loss of acid sites. K_2O can coordinate with the acid sites on the surface of the catalysts and neutralize their acidity, reducing the amount of NH_3 adsorbed on these acid sites. Consequently, NH_3 is more likely to adsorb on the redox sites or react with O_2 to produce undesired by-products, resulting in a decrease in N_2 selectivity. Even though the oxidation ability is somewhat suppressed after K_2O poisoning in these catalysts, the N_2 selectivity still declines due to an insufficient number of NH_3 adsorption acid sites.

Common understanding holds that the low-temperature activity of catalysts is often determined by their redox properties. Referring back to Fig. 2, the changes in activity over the poisoned catalysts can be well explained based on the results in Fig. 3B. Due to the enhanced oxidation ability, the low-temperature activity increases after K_2O poisoning over the MnO_x catalysts. Conversely, due to the decreased oxidation ability, the low-temperature activity decreases after K_2O poisoning over the $\text{Mn}_{0.90}\text{Mo}_{0.09}\text{V}_{0.01}\text{O}_x$ and $\text{Mn}_{0.90}\text{Mo}_{0.10}\text{O}_x$ catalysts. The K_2O poisoning effect is insignificant on $\text{Mn}_{0.90}\text{V}_{0.10}\text{O}_x$ catalysts, therefore, $\text{Mn}_{0.90}\text{V}_{0.10}\text{O}_x\text{-K}$ shows almost the same low-temperature activity as the fresh one. The results of the separate NH_3 oxidation align well with the K-resistance performance in Fig. 2. The changes of redox property of the catalysts will be further confirmed by the latter $\text{H}_2\text{-TPR}$ analysis.

It has been discovered that increasing the catalytic activity of the SCR catalyst for NO oxidation to NO_2 can significantly spending up its low-temperature SCR performance due to the occurrence of "fast SCR" [1]. Therefore, the separated NO oxidation reactions are carried out over the fresh catalysts. As shown in Fig. 3C, MnO_x displays the best NO oxidation ability, converting more NO into NO_2 . However, the NO oxidation ability is significantly inhibited after Mo tuning, especially the co-tuning of Mo and V. The highest NO to NO_2 conversion (53%) could be realized at only 325 °C on MnO_x , but the highest NO to NO_2 conversions (less than 18%) are achieved at the temperature higher than 425 °C on the regulated ternary catalysts. The NO oxidation results are in consistent with the separate NH_3 oxidation performance (Fig. 3A), indicating that better NH_3 oxidation performance corresponds to better NO oxidation performance. This further confirms that the co-tuning of Mo and V on MnO_x can indeed restrict the oxidation ability. Moreover, separate NO oxidation reactions are also performed on the K_2O -poisoned catalysts and are displayed in Fig. 3D. As expected, $\text{MnO}_x\text{-K}$ exhibits higher NO oxidation performance than the fresh catalyst. However, both the NO to NO_2 conversions decline to some extent over the other poisoned catalysts due to their lower oxidation ability. It may appear contradictory that MnO_x , despite showing higher NO to NO_2 conversion and higher NO_2 concentration during the separate NO oxidation reaction, has worse low-temperature $\text{NH}_3\text{-SCR}$ activity than ternary $\text{Mn}_{0.90}\text{Mo}_\delta\text{V}_{0.10-\delta}\text{O}_x$ ($\delta = 0.01, 0.03, 0.05, 0.07, 0.09$) catalysts. The reason for this lies in the fact that the SCR reaction over the catalysts

does not solely depend on the oxidation of NO to NO_2 (or NO activation). Instead, during the low-temperature SCR reaction, the reaction between gaseous NO_x (including NO and NO_2) and adsorbed NH_3 species may be the rate-determining step [43]. Moreover, the acid sites also play an essential role in the excellent low-temperature activity of the catalyst. It is worth noting that both the NO to NO_2 oxidation activity is restrained over the fresh and poisoned ternary $\text{Mn}_{0.90}\text{Mo}_\delta\text{V}_{0.10-\delta}\text{O}_x$ ($\delta = 0.01, 0.03, 0.05, 0.07, 0.09$) catalysts, yet they still show considerable $\text{NH}_3\text{-SCR}$ activity in the medium-high temperature range (Fig. 1 and Fig. 2). This suggests that over the Mo and V co-modified MnO_x catalyst, NO can directly participate in the $\text{NH}_3\text{-SCR}$ reaction in the gas phase without the need to adsorb onto the catalyst surface as nitrites or nitrates. Subsequent in situ DRIFTS characterization results will confirm this. Based on the above separate NH_3 and NO oxidation results discussed above, it becomes evident that the co-tuning of Mo and V on the MnO_x catalyst significantly inhibits both NH_3 and NO oxidation abilities of the ternary $\text{Mn}_{0.90}\text{Mo}_\delta\text{V}_{0.10-\delta}\text{O}_x$ ($\delta = 0.01, 0.03, 0.05, 0.07, 0.09$) catalysts.

3.4. Physicochemical characteristics over the catalysts

The morphology of all fresh catalysts, including MnO_x , $\text{Mn}_{0.90}\text{Mo}_{0.10}\text{O}_x$, $\text{Mn}_{0.90}\text{V}_{0.10}\text{O}_x$, and the ternary $\text{Mn}_{0.90}\text{Mo}_\delta\text{V}_{0.10-\delta}\text{O}_x$ ($\delta = 0.01, 0.03, 0.05, 0.07, 0.09$) catalysts, are investigated using SEM technology and showed in Fig. S7. These catalysts consist of small particles, with MnO_x displaying a smooth surface and the other tuned catalysts exhibiting relatively rough surfaces. Notably, some significantly larger particles (> 500 nm) were observed in $\text{Mn}_{0.90}\text{Mo}_{0.01}\text{V}_{0.09}\text{O}_x$, $\text{Mn}_{0.90}\text{Mo}_{0.03}\text{V}_{0.07}\text{O}_x$, and $\text{Mn}_{0.90}\text{Mo}_{0.07}\text{V}_{0.03}\text{O}_x$ catalysts. To explore the effect of K-poisoning on morphology, the poisoned catalysts were also characterized via SEM, as displayed in Fig. S8. In comparison with the fresh catalysts, the morphologies of the poisoned catalysts show minimal changes, indicating that K-poisoning may not significantly alter the morphology of the catalyst. Moreover, the structure morphologies of MnO_x , $\text{Mn}_{0.90}\text{Mo}_{0.10}\text{O}_x$, $\text{Mn}_{0.90}\text{V}_{0.10}\text{O}_x$, $\text{Mn}_{0.90}\text{Mo}_{0.09}\text{V}_{0.01}\text{O}_x$, and $\text{Mn}_{0.90}\text{Mo}_{0.09}\text{V}_{0.01}\text{O}_x\text{-K}$ catalysts are further visualized by TEM, as shown in Fig. 4 (A – E). The outcomes provide further evidences that the catalysts are made up of many particles. MnO_x exhibited an average particle size of 220 nm, which significantly decreased after tuning with V, particularly Mo, resulting in particle sizes of 167 nm and 28 nm for $\text{Mn}_{0.90}\text{V}_{0.10}\text{O}_x$ and $\text{Mn}_{0.90}\text{Mo}_{0.10}\text{O}_x$, respectively. The ternary $\text{Mn}_{0.90}\text{Mo}_{0.09}\text{V}_{0.01}\text{O}_x$ also have much smaller particle size (33 nm) than that of MnO_x . Consequently, it can be concluded that co-tuning Mo and V on MnO_x effectively reduces the particle size of the catalysts. Smaller catalyst particles typically translate to a larger specific surface area and more exposed active sites, which may contribute to the superior $\text{NH}_3\text{-SCR}$ performance of the tuned $\text{Mn}_{0.90}\text{Mo}_{0.09}\text{V}_{0.01}\text{O}_x$ catalyst in comparison to pure MnO_x . After K-poisoning, the average particle size of $\text{Mn}_{0.90}\text{Mo}_{0.09}\text{V}_{0.01}\text{O}_x\text{-K}$ increased to 42 nm, slightly higher than that of the fresh catalyst. The HAADF-STEM image (Fig. 4F) and the associated elemental EDS mapping images are presented in Fig. 4 (G–K), indicating that the Mn, Mo, V, and O elements are evenly distributed throughout over the $\text{Mn}_{0.90}\text{Mo}_{0.09}\text{V}_{0.01}\text{O}_x\text{-K}$ catalyst.

To investigate the impact of co-tuning of Mo and V on the crystal structure of MnO_x , XRD analysis was conducted on various fresh catalysts. The results, depicted in Fig. 5A, reveal that MnO_x exhibits characteristic diffraction peaks of Mn_2O_3 (JCPDS PDF #24-0508). Upon Mo tuning, the diffraction peaks of Mn_2O_3 diminish, and new crystalline phases of MnMoO_4 (JCPDS PDF #50-1287) and Mn_3O_4 (JCPDS PDF #18-0803) emerge in the $\text{Mn}_{0.90}\text{Mo}_{0.10}\text{O}_x$ catalyst. Following V tuning, the diffraction peaks of Mn_2O_3 (JCPDS PDF #50-1287) and Mn_3O_4 (JCPDS PDF #18-0803) are observed on the $\text{Mn}_{0.90}\text{V}_{0.10}\text{O}_x$ catalyst. In the case of ternary $\text{Mn}_{0.90}\text{Mo}_\delta\text{V}_{0.10-\delta}\text{O}_x$ ($\delta = 0.01, 0.03, 0.05, 0.07, 0.09$) catalysts, three crystalline phases, Mn_2O_3 (JCPDS PDF #41-1442), Mn_3O_4 (JCPDS PDF #18-0803), and MnMoO_4 (JCPDS PDF #50-1287), are detected. Notably, no diffraction peaks related to V species are observed over all catalysts, indicating the highly dispersed nature of the

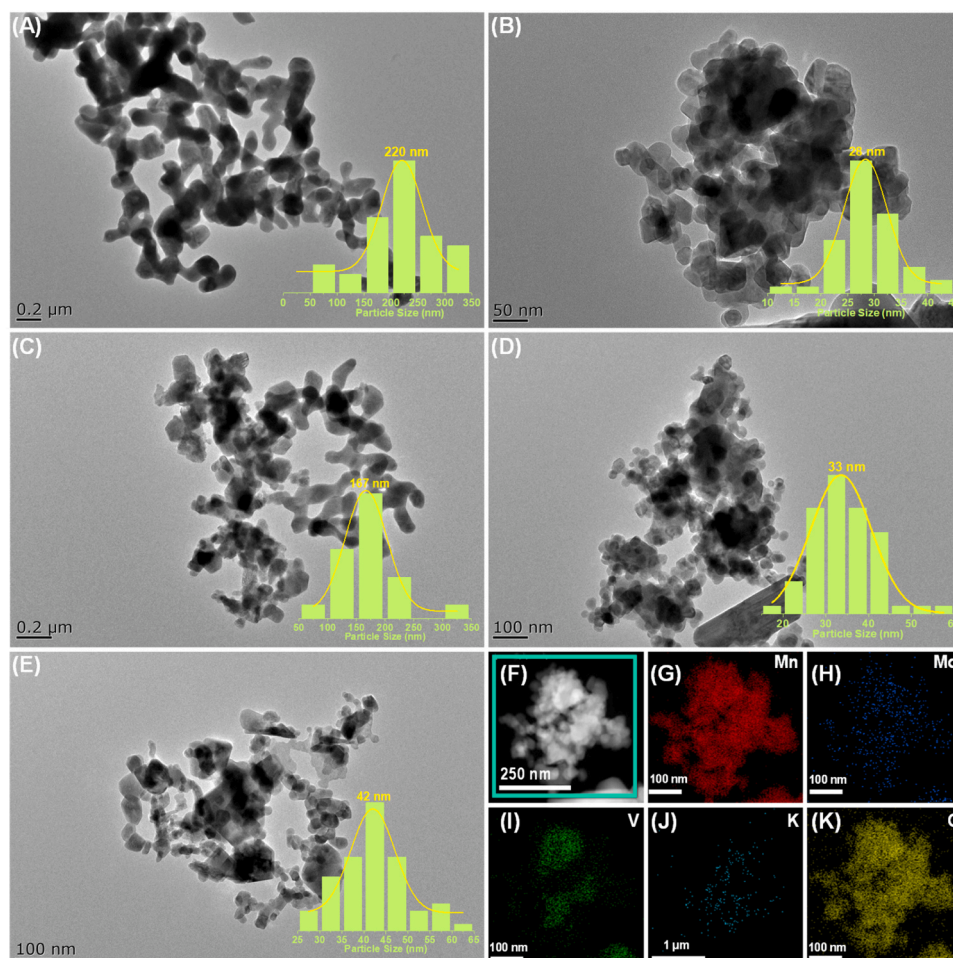


Fig. 4. The TEM images of the catalysts (A: MnO_x , B: $\text{Mn}_{0.90}\text{Mo}_{0.10}\text{O}_x$, C: $\text{Mn}_{0.90}\text{V}_{0.10}\text{O}_x$, D: $\text{Mn}_{0.90}\text{Mo}_{0.09}\text{V}_{0.01}\text{O}_x$, E: $\text{Mn}_{0.90}\text{Mo}_{0.09}\text{V}_{0.01}\text{O}_x\text{-K}$); (F) High-angle annular dark field image and (G – K) EDS mappings of the $\text{Mn}_{0.90}\text{Mo}_{0.09}\text{V}_{0.01}\text{O}_x\text{-K}$ catalyst.

V species. It is highlighting that peak intensities significantly diminish after Mo and/or V tuning on MnO_x , suggesting a reduction in crystallinity. To assess the influence of K-poisoning on crystalline phases, the poisoned catalysts were subjected to XRD analysis, as shown in Fig. S9. The positions of characteristic diffraction peaks remained relatively stable, with no new phases detected post K-poisoning. To gain further insights into the composition of the prepared catalysts, Raman spectra were recorded. As depicted in Fig. 5B, the band located at 631 cm^{-1} is attributed to the Mn–O breathing vibration of divalent manganese ions in tetrahedral coordination over the MnO_x sample [44]. Following tuning with Mo and/or V, this Raman peak exhibits a noticeable shift toward higher wavenumber regions, indicating the emergence of interactions between Mn and other metal elements. On all V-containing catalysts, the Raman bands at 831 cm^{-1} are ascribed to the vibration of Mn–O–V [45], indicating that Mn and V can combine to form metal oxides after tuning MnO_x with V. However, the vibration of Mn–O–V is hardly observed over the $\text{Mn}_{0.90}\text{Mo}_{0.09}\text{V}_{0.01}\text{O}_x$ catalyst due to the very little V content. On all Mo-containing catalysts, the Raman bands centered at approximately 921 cm^{-1} correspond to the characteristic features of MnMoO_4 [46,47], which is consistent with the XRD findings mentioned above. However, the characteristic band of MnMoO_4 is hardly detected over the $\text{Mn}_{0.90}\text{Mo}_{0.01}\text{V}_{0.09}\text{O}_x$ catalyst due to its minimal Mo content. According to the XRD results, it can be concluded that portion of Mn_2O_3 can be converted into Mn_3O_4 specie, and Mn can combine with Mo or V to create stable MnMoO_4 or Mn–O–V species, respectively. It is generally known that Mn_3O_4 possesses lower oxidation ability compared to Mn_2O_3 [42,48], so the catalysts tuned with Mo and

V exhibit the lower oxidation capacity than that of pure MnO_x . This explanation provides a reasonable basis for understanding why MnO_x demonstrates stronger separate NH_3 and NO oxidation abilities (Fig. 3A, C). Another contributing factor to the decline in oxidation ability among the tuned catalysts is the formation of highly stable bimetallic oxides, where Mn coordinates with V, particularly Mo. Further elaboration on this phenomenon will be provided in the subsequent H_2 -TPR analysis.

The N_2 adsorption-desorption results for the fresh catalysts are shown in Fig. 5C. All catalysts exhibit "type IV" N_2 adsorption-desorption isotherm curves with type H3 hysteresis loops, indicating a mesoporous structure created by particle accumulation [49]. Table S4 presents the BET surface areas of all synthesized samples. MnO_x possesses the smallest surface area at only $6\text{ m}^2\text{ g}^{-1}$. However, after modification with V, particularly Mo, the specific surface area significantly increases, with $\text{Mn}_{0.90}\text{V}_{0.10}\text{O}_x$ and $\text{Mn}_{0.90}\text{Mo}_{0.10}\text{O}_x$ reaching 11 and $20\text{ m}^2\text{ g}^{-1}$, respectively. In contrast, $\text{Mn}_{0.90}\text{Mo}_{0.01}\text{V}_{0.09}\text{O}_x$, $\text{Mn}_{0.90}\text{Mo}_{0.03}\text{V}_{0.07}\text{O}_x$, and $\text{Mn}_{0.90}\text{Mo}_{0.07}\text{V}_{0.03}\text{O}_x$ show relatively smaller surface area among all the ternary catalysts due to the formation of significantly larger particles, which are in accordance with the above electron microscopic characterizations. Overall, the co-tuning of Mo and V on MnO_x leads to ternary $\text{Mn}_{0.90}\text{Mo}_\delta\text{V}_{1-\delta}\text{O}_x$ ($\delta = 0.01, 0.03, 0.05, 0.07, 0.09$) catalysts maintain relatively higher specific surface areas. This, in turn, provides more active and adsorption sites, ultimately contributing to enhanced NH_3 -SCR activity. The N_2 adsorption-desorption results for the poisoned catalysts, as shown in Fig. S10, reveal that the types of N_2 adsorption-desorption isotherm curves remain unchanged. Furthermore, the BET surface area over the poisoned catalysts undergoes

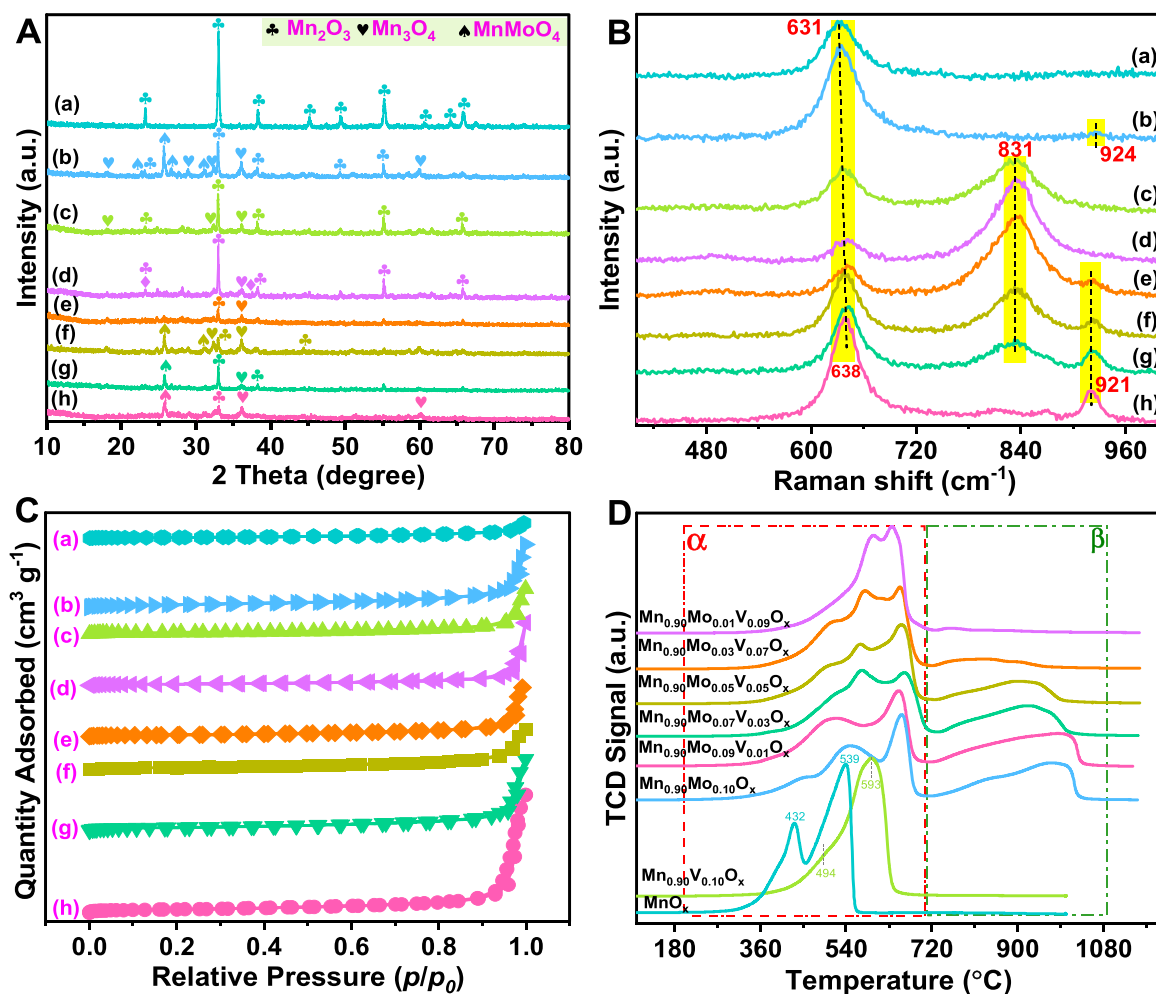


Fig. 5. (A) The powder XRD patterns, (B) Raman spectra and (C) N_2 adsorption-desorption isotherms (a: MnO_x , b: $\text{Mn}_{0.90}\text{Mo}_{0.01}\text{V}_{0.09}\text{O}_x$, c: $\text{Mn}_{0.90}\text{Mo}_{0.03}\text{V}_{0.07}\text{O}_x$, d: $\text{Mn}_{0.90}\text{Mo}_{0.05}\text{V}_{0.05}\text{O}_x$, e: $\text{Mn}_{0.90}\text{Mo}_{0.07}\text{V}_{0.03}\text{O}_x$, f: $\text{Mn}_{0.90}\text{Mo}_{0.09}\text{V}_{0.01}\text{O}_x$, g: $\text{Mn}_{0.90}\text{Mo}_{0.10}\text{O}_x$, h: MnO_x), and (D) H_2 -TPR profiles of the various fresh catalysts.

minimal change, with the decline being negligible (Table S4). This suggests that K_2O poisoning has a limited effect on the textural properties of the catalysts.

The redox ability of the fresh catalysts is investigated through H_2 -TPR, as illustrated in Fig. 5D. MnO_x displays two reduction peaks at 432 and 539 $^\circ\text{C}$, respectively. These peaks are attributed to the stepwise reduction of Mn_2O_3 to Mn_3O_4 and ultimately to MnO [50,51]. After tuning with V, two reduction peaks emerge at 494 and 593 $^\circ\text{C}$, the former is ascribed to the reduction of Mn_2O_3 and the latter peak is attributed the overlapping reduction Mn_3O_4 and V-containing (such as $\text{Mn}-\text{VO}_x$, VO_x , etc.) species [52]. In comparison to MnO_x , both reduction peaks shift to higher temperatures in the $\text{Mn}_{0.90}\text{V}_{0.10}\text{O}_x$ catalyst, indicating a decline in its reducibility and a decrease in the oxidation ability of MnO_x after V tuning. Regarding other catalysts, the H_2 -TPR curves can be divided into two regions, that is α (< 710 $^\circ\text{C}$) and β region (> 710 $^\circ\text{C}$), respectively. The α region is corresponded to the overlapping reduction of Mn_2O_3 , Mn_3O_4 , and V-containing species (except $\text{Mn}_{0.90}\text{Mo}_{0.10}\text{O}_x$), while the β region is assigned to the reduction of MnMoO_4 . Notably, MnMoO_4 is challenging to reduce, indicating poor oxidation capacity. The onset of H_2 uptake (200 – 400 $^\circ\text{C}$) are also investigated and shown in Fig. S11A. The initial H_2 uptakes are evidently restricted over the tuned catalysts, further confirming the lower oxidation ability of these tuned catalysts. Based on the above H_2 -TPR results, it can be concluded that the main reduction peaks shift to much higher temperature, and the initial H_2 uptakes are constrained

compared to pure MnO_x after tuning MnO_x with Mo and V. This indicates that the oxidation ability can be effectively inhibited through this tuning method, aligning with the separate NH_3 oxidation and NO results over the fresh catalysts (Fig. 3A, C). It is worth noting that, as shown in Fig. S11B, although $\text{Mn}_{0.90}\text{Mo}_{0.09}\text{V}_{0.01}\text{O}_x$ exhibits significantly weaker oxidative ability compared to MnO_x , it still possesses the strongest oxidative capacity among all the regulated series of ternary $\text{Mn}_{0.90}\text{Mo}_\delta\text{V}_{0.10-\delta}\text{O}_x$ ($\delta = 0.01, 0.03, 0.05, 0.07, 0.09$) catalysts. This is one of the important factors contributing to its excellent low-temperature NH_3 -SCR performance. Properly reducing the oxidative capacity of the catalyst is advantageous for the NH_3 -SCR reaction, but completely eliminating its oxidative ability is unwise. The catalyst performs most favorably for the smooth progression of the NH_3 -SCR reaction when it exhibits moderate oxidative capability.

Moreover, to investigate the impact of K_2O poisoning on the catalyst's redox ability, H_2 -TPR tests were also conducted on the poisoned catalysts and are presented in Fig. S12. Compared with the fresh catalysts (green line), the peaks attributed to the overlapping reduction of Mn_2O_3 , Mn_3O_4 , and V-containing species of the K_2O -poisoned catalysts (pink line) shift to higher temperatures. The shifts indicate weaker oxidation ability in these poisoned catalysts. However, something different occurred with the MnO_x -K catalyst, where the two reduction peaks shifted to lower temperatures, implying a stronger oxidation capacity after K_2O poisoning. As for the $\text{Mn}_{0.90}\text{V}_{0.10}\text{O}_x$ -K catalyst, the position of the reduction peak hardly changed, suggesting that the

oxidation ability of the catalyst remained relatively unchanged. These results align with the previously discussed separate NO and NH₃ oxidation results over the poisoned catalysts (Fig. 2B, D). Besides, we had previously speculated that the changes in low-temperature NH₃-SCR and NH₃ (or NO) oxidation performance over the poisoned catalysts could be attributed to changes in oxidation ability, and the H₂-TPR results of the poisoned catalysts confirm the hypothesis in Fig. 3. It is generally believed that the low-temperature activity of catalyst is usually determined by its redox properties, and the results in this work are in accordance with this viewpoint. After K₂O poisoning, the oxidation ability enhances in the MnO_x-K catalyst, resulting in some improvements in low-temperature NH₃-SCR activity. After K₂O-poisoning, the oxidation ability remains almost unchanged in the Mn_{0.90}V_{0.10}O_x-K catalyst, resulting in little change in its low-temperature NH₃-SCR activity. But for other catalysts, the oxidation abilities are weakened after K₂O poisoning, leading to decreases in activity to a certain extent. Notably, as depicted in Fig. S13, despite the reduced oxidative performance of the series of catalysts after K poisoning, Mn_{0.90}Mo_{0.09}V_{0.01}O_x-K still exhibits the strongest oxidative capability among all the ternary Mn_{0.90}Mo_δV_{0.10-δ}O_x-K (δ = 0.01, 0.03, 0.05, 0.07, 0.09) catalysts, consistent with its superior NH₃-SCR performance.

XPS experiments were conducted to explore the chemical states of surface species and the types of oxygen species over fresh and poisoned samples. As shown in Fig. S14, after performing peak-fitting deconvolution, the Mn 2p_{3/2} peak can be divided into three peaks, corresponding to Mn²⁺ (640.3–640.7 eV), Mn³⁺ (641.6–642.3 eV) and Mn⁴⁺ (643.2–644.5 eV) [53,54]. Mn⁴⁺ typically assumes an indispensable role in SCR reaction. The redox cycle exhibited by Mn⁴⁺ species notably enhances SCR performance under lower temperature conditions, primarily due to its facilitation of the oxidation process from NO to NO₂ [55]. Therefore, in general, the higher the proportion of Mn⁴⁺ in the catalyst, the better its low-temperature activity. Furthermore, the proportion of surface-adsorbed oxygen species (O_s) in the catalyst is also a crucial factor influencing the oxidation capacity. The main signals of oxygen species were defined through the peak-fitting deconvolution in Fig. S15. The peak located at 529.3–530.7 eV can be assigned to the lattice oxygen species (O_L), while O_s is corresponded to the peak of 530.9–531.9 eV, and surface OH groups at 533.1–532.9 eV, probably resulting from chemisorbed water (O_W) [56,57]. As listed in the Table S5, the MnO_x possesses the highest proportion of Mn⁴⁺ and O_s, directly corresponding to its strongest capability for oxidizing NO to NO₂ (Fig. 3C), as well as its highest oxidation capacity (Fig. 3A and H₂-TPR results). Following the modification of MnO_x by either Mn or V, there is a decrease in the proportions of Mn⁴⁺ and O_s over the binary catalysts. However, the reduction is more significant with V addition, indicating that the introduction of V is more effective in inhibiting the oxidation capacity. For the ternary Mn_{0.90}Mo_δV_{0.10-δ}O_x (δ = 0.01, 0.03, 0.05, 0.07, 0.09) catalysts tuned simultaneously with Mo and V, their Mn⁴⁺ proportions are decreased compared to MnO_x, resulting in diminished oxidation capabilities. However, Mn_{0.90}Mo_{0.09}V_{0.01}O_x, which only exhibits slightly reduced proportions of Mn⁴⁺ and O_s compared to other ternary catalysts, maintains the highest levels among all tuned catalysts. This preservation of strong oxidation capability significantly contributes to its excellent activity.

The XPS analysis of V and Mo species on the surface of the fresh catalysts are presented in Fig. S16 and Fig. S17, respectively. In all analyzed catalysts, two peaks are observed in V 2p_{3/2} spectra. The peaks at binding energies of 517.3±0.4 and 516.6±0.4 eV are ascribed to V⁵⁺ and V⁴⁺, respectively [58]. Table S5 highlights that the V species primarily exist in the form of V⁵⁺. The Mo 3d XPS spectrum shows a 3d_{5/2}–3d_{3/2} doublet at 231.9 and 235 eV, respectively. The observed binding energy and the splitting width (ΔMo 3d = 3.1 eV) are consistent with previously reported values for Mo⁶⁺ [59]. Moreover, the XPS analysis over the K-poisoned catalysts is also conducted (Fig. S18–S21) and listed in Table S5. After K poisoning, the proportions of Mn⁴⁺ and O_s in the MnO_x-K both increase, accounting for the improvement in its

oxidation performance. Regarding other binary or ternary catalysts post-poisoning, there is minimal change in the Mn⁴⁺ proportion, while the ratios of O_s exhibit a reduction. The reduction in O_s is the primary reason behind the diminished oxidation capability of the poisoned catalyst. Additionally, the proportion of V⁵⁺ in the poisoned catalysts also decreases, contributing to a certain extent to the weakening of the oxidation capacity of the catalysts. Despite the decrease in Mn⁴⁺ and O_s proportions over the Mn_{0.90}Mo_{0.09}V_{0.01}O_x catalyst after poisoning, it still remains the highest among all poisoned ternary catalysts, ensuring it retains a considerably strong oxidation capacity.

We have established that the oxidation ability is suppressed after the tuning of Mo and V on MnO_x catalyst. However, the low-temperature activities and the active temperature windows of the ternary Mn_{0.90}Mo_δV_{0.10-δ}O_x (δ = 0.01, 0.03, 0.05, 0.07, 0.09) catalysts are superior to that of MnO_x, which might appear contradictory. This is mainly because of the significant role played by acid sites. During NH₃-SCR processes, the acid sites and redox sites do not function independently; rather, the exceptional performance of the catalyst is a result of their collaborative action. Therefore, it becomes imperative to study the acid properties of the catalysts, and NH₃-TPD-MS tests were conducted to shed light on this aspect. As shown in Fig. 6, the peaks around 150 °C can be attributed NH₃ adsorbed to the weak acid sites, while the peaks around 200–350 °C are associated with medium-strong acid sites [39]. By integrating the desorption peaks and normalizing the desorbed NH₃ amounts, the results presented in Table S6 indicate that pure MnO_x possesses a very low acid amount, only 9.1 μmol g⁻¹. However, when using Mo and V to regulate MnO_x, both the quantity and strength of the acid sites within the catalyst are obviously enhanced. The enhancement elucidates why the catalyst can maintain exceptionally high catalytic activity despite the weakening of its oxidative performance, especially with a significant improvement in its high-temperature activity. It is important to highlight that, despite Mn_{0.90}Mo_{0.01}V_{0.09}O_x having the highest number of acid sites based on the NH₃-TPD-MS results, it exhibits the lowest proportions of Mn⁴⁺ and O_s, resulting in the weakest oxidation capability, which aligns with the findings of the H₂-TPR findings (Fig. S11). The limited oxidation capacity of Mn_{0.90}Mo_{0.01}V_{0.09}O_x severely hinders its performance in NH₃-SCR. Among all the series of regulated Mn_{0.90}Mo_δV_{0.10-δ}O_x (δ = 0.01, 0.03, 0.05, 0.07, 0.09) catalysts, it is noteworthy that the Mn_{0.90}Mo_{0.09}V_{0.01}O_x catalyst, while not having the highest quantity of acid sites, exhibits the highest NH₃-SCR activity. This is primarily attributed to its relatively stronger oxidation ability. It is the combination of a moderate oxidative capacity and enough number of acid sites that ensures its exceptional activity.

Furthermore, NH₃-TPD-MS tests were conducted on the poisoned catalysts to investigate the impact of K poisoning on their surface acidity, and the results are presented in Fig. S22 and Table S6. Evidently, over the MnO_x-K catalyst, the total acid site content decreases significantly by 12.1% after poisoning. This elucidates why, despite a slight improvement in its oxidation ability, the medium-high temperature activity notably declines. This decline can be attributed to the heightened importance of acid sites in catalysts at medium-high temperatures. For other poisoned catalysts (excluding Mn_{0.90}Mo_{0.09}V_{0.01}O_x-K), not only does the quantity of acid sites decrease significantly, but the NH₃ desorption peak also notably shifts towards lower temperatures. This suggests that K poisoning not only reduces the number of acid sites but also weakens their strength. Combined with the previously established evidence that K poisoning impairs the oxidation ability of the catalyst, it can be concluded that the dual detrimental effect on acid sites and oxidation capability leads to a significant decline in catalytic performance after poisoning. It is worth noting that for the Mn_{0.90}Mo_{0.09}V_{0.01}O_x-K catalyst, the reduction in the quantity of acid sites after K poisoning is relatively low, at 6.6%. Furthermore, after K poisoning, there is almost no change in the NH₃ desorption peak temperature, indicating that despite the decrease in the number of acidic sites, its acidity remains largely intact. Combining the previous H₂-TPR analysis results (Fig. S13), it can be inferred that the K-poisoned

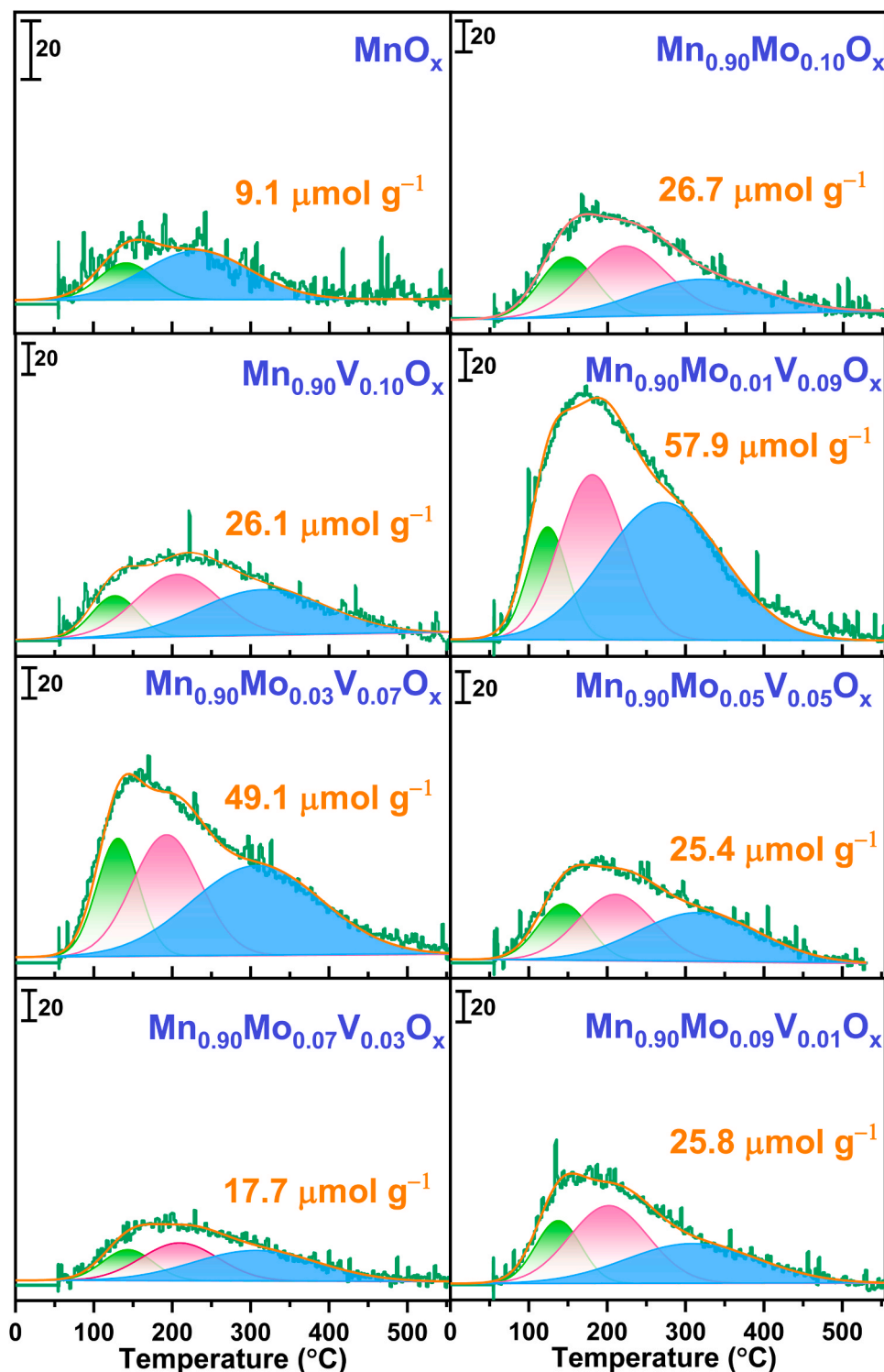


Fig. 6. The NH_3 -TPD-MS profiles over fresh MnO_x , $\text{Mn}_{0.90}\text{Mo}_{0.10}\text{O}_x$, $\text{Mn}_{0.90}\text{V}_{0.10}\text{O}_x$ and $\text{Mn}_{0.90}\text{Mo}_\delta\text{V}_{0.10-\delta}\text{O}_x$ ($\delta = 0.01, 0.03, 0.05, 0.07, 0.09$) catalysts.

$\text{Mn}_{0.90}\text{Mo}_{0.09}\text{V}_{0.01}\text{O}_x$ -K still possesses a relatively robust oxidation ability and a significant number of acid sites with high surface acidity. It is precisely for this reason that it exhibits the best NH_3 -SCR catalytic activity among all the poisoned catalysts.

Combining the findings from H_2 -TPR, XPS and NH_3 -TPD-MS analyses above, it becomes evident that the introduction of Mo and V into MnO_x enables the precise regulation of catalytic acid and redox sites. When the proportions between Mn, Mo, and V are appropriately balanced, the catalyst exhibits superior NH_3 -SCR performance. This is primarily

attributed to the regulating influence of Mo and V, which effectively fine-tune the oxidation capacity of the catalyst, resulting in a moderate oxidation ability and a sufficient number of acid sites. Furthermore, it is apparent that the oxidative capacity of a catalyst and the abundance of acidic sites do not necessarily adhere to the "stronger is better" trend. Rather, it is the harmonious balance between these two factors that serves as the pivotal determinant of the NH_3 -SCR catalytic performance.

3.5. Mechanisms for catalytic reduction of NO_x

To explore whether the regulation of Mn and V on MnO_x alters the NH_3 -SCR catalytic reaction mechanism, in situ DRIFT spectra experiences were performed over the typical catalysts. NH_3 adsorption constitutes the initial stage in the NH_3 -SCR reaction, making the behavior of NH_3 adsorption of significant importance in this process. Figs. 7A and 7B display the in situ time-resolved DRIFT spectra of NH_3 adsorption over MnO_x and $\text{Mn}_{0.90}\text{Mo}_{0.09}\text{V}_{0.01}\text{O}_x$ at 100°C , respectively. For pure MnO_x sample (Fig. 7A), two peaks located at 1302 and 1193 cm^{-1} are ascribed

to coordinated NH_3 species and NH_3 coordinated with Lewis acid sites ($\text{NH}_3\text{-L}$), respectively [60,61]. Compared with the NH_3 adsorption behavior on MnO_x , significant changes are observed on the $\text{Mn}_{0.90}\text{Mo}_{0.09}\text{V}_{0.01}\text{O}_x$ sample (Fig. 7B), not only are $\text{NH}_3\text{-L}$ (1193 cm^{-1}) species detected, but new NH_4^+ species bounded to Brønsted acid sites ($\text{NH}_4^+\text{-B}$, 1430 cm^{-1}) are also detected [56]. Moreover, the peak corresponding to $\text{NH}_3\text{-L}$ or $\text{NH}_4^+\text{-B}$ in $\text{Mn}_{0.90}\text{Mo}_{0.09}\text{V}_{0.01}\text{O}_x$ has a significantly higher peak area and peak intensity compared to MnO_x , indicating that the former possesses more Lewis and Brønsted acid sites. As widely recognized, Brønsted acid sites are more favorable for low-temperature

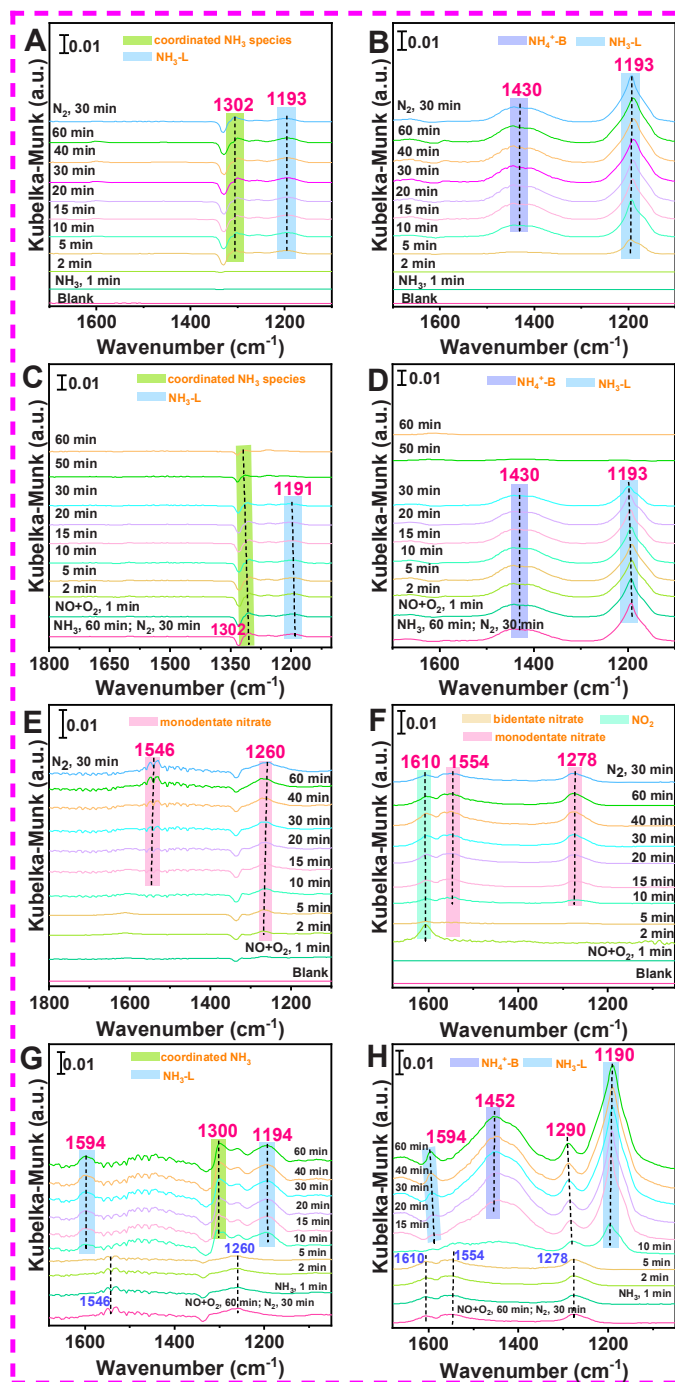


Fig. 7. In situ DRIFT spectra of NH_3 adsorption over (A) MnO_x and (B) $\text{Mn}_{0.90}\text{Mo}_{0.09}\text{V}_{0.01}\text{O}_x$ catalysts at 100°C ; In situ DRIFT spectra of pre-adsorbed NH_3 species reacted with $\text{NO} + \text{O}_2$ over (C) MnO_x and (D) $\text{Mn}_{0.90}\text{Mo}_{0.09}\text{V}_{0.01}\text{O}_x$ catalysts at 100°C ; In situ DRIFT spectra of $\text{NO} + \text{O}_2$ adsorption over (E) MnO_x and (F) $\text{Mn}_{0.90}\text{Mo}_{0.09}\text{V}_{0.01}\text{O}_x$ catalysts at 100°C ; In situ DRIFT spectra of pre-adsorbed $\text{NO} + \text{O}_2$ reacted with NH_3 over (G) MnO_x and (H) $\text{Mn}_{0.90}\text{Mo}_{0.09}\text{V}_{0.01}\text{O}_x$ catalysts at 100°C .

SCR activity [41]. Consequently, despite some inhibition in the redox properties of the $\text{Mn}_{0.90}\text{Mo}_{0.09}\text{V}_{0.01}\text{O}_x$ catalyst, it still demonstrated outstanding performance at low temperatures. Moreover, the formation of a greater number of Lewis acid sites on $\text{Mn}_{0.90}\text{Mo}_{0.09}\text{V}_{0.01}\text{O}_x$ catalyst is also advantageous for its adsorption of NH_3 at medium-high temperatures [62]. Thus, $\text{Mn}_{0.90}\text{Mo}_{0.09}\text{V}_{0.01}\text{O}_x$ not only exhibits excellent low-temperature activity but also demonstrates superior high-temperature activity compared to MnO_x .

The reactivity of pre-adsorbed NH_3 with $\text{NO} + \text{O}_2$ was investigated over the MnO_x and $\text{Mn}_{0.90}\text{Mo}_{0.09}\text{V}_{0.01}\text{O}_x$ catalysts at 100°C . Firstly, NH_3 species were pre-adsorbed onto the MnO_x catalyst for 60 min and then purged with N_2 for 30 min before introducing $\text{NO} + \text{O}_2$ mixed gases. As shown in Fig. 7C, for MnO_x catalyst, the band at 1191 cm^{-1} attributed to $\text{NH}_3\text{-L}$ decreased slowly and vanished completely within 50 min when exposed to a $\text{NO} + \text{O}_2$ atmosphere. However, the band at 1302 cm^{-1} ascribed to coordinated NH_3 species gradually decreased with the introduction of the $\text{NO} + \text{O}_2$ atmosphere, but it can still be detected after 60 min, indicating that coordinated NH_3 species had not been completely consumed. Similarly, a same experimental procedure was applied to $\text{Mn}_{0.90}\text{Mo}_{0.09}\text{V}_{0.01}\text{O}_x$ catalyst. As shown in Fig. 7D, while the peak intensities and areas attributed to $\text{NH}_3\text{-L}$ or $\text{NH}_4^+\text{-B}$ on $\text{Mn}_{0.90}\text{Mo}_{0.09}\text{V}_{0.01}\text{O}_x$ are significantly higher compared to MnO_x catalyst, their consumption rates are also faster. After 50 min of exposure to $\text{NO} + \text{O}_2$ atmosphere, $\text{NH}_3\text{-L}$ and $\text{NH}_4^+\text{-B}$ species are no longer detectable, and subsequently, no characteristic peaks related to any N-containing species (such as nitrate, nitrite, and NO_2) can be observed. The subsequent each data plot almost shows a straight line, which indicates that NO is difficult to adsorb onto the catalyst that pre-treated with NH_3 . Thus, the regulation of MnO_x by Mo and V significantly enhances the reaction rate between adsorbed ammonia species and gaseous NO , which is a crucial factor contributing to the superior low-temperature activity of $\text{Mn}_{0.90}\text{Mo}_{0.09}\text{V}_{0.01}\text{O}_x$ when compared to pure MnO_x .

Figs. 7E and 7F show the NO_x adsorption ability of MnO_x and $\text{Mn}_{0.90}\text{Mo}_{0.09}\text{V}_{0.01}\text{O}_x$, respectively. After $\text{NO} + \text{O}_2$ adsorption and N_2 purge at 100°C , only the infrared bands attributed to monodentate nitrate (1546 and 1260 cm^{-1}) appeared on the surface of MnO_x (Fig. 7E) [28,63]. However, on catalyst $\text{Mn}_{0.90}\text{Mo}_{0.09}\text{V}_{0.01}\text{O}_x$ (Fig. 7F), not only was monodentate nitrate (1278 and 1554 cm^{-1}) detected [28,40], but the weak adsorption of NO_2 (1610 cm^{-1}) was also observed [54]. Reaction between adsorbed $\text{NO} + \text{O}_2$ and NH_3 species was performed over the above two catalysts at 100°C and the corresponding results are shown in Fig. 7 (G and H). Initially, the sample was subjected to $\text{NO} + \text{O}_2$ gas exposure for 60 min, followed by a 30 min N_2 purging. Subsequently, NH_3 was introduced, and the relevant spectra were recorded at various time intervals. As shown in Fig. 7G, after introducing NH_3 into the IR cell, the band intensity of corresponding monodentate nitrate (1260 and 1546 cm^{-1}) decreased slowly and vanished after 10 min. As NH_3 continued to be introduced, coordinated NH_3 species (1300 cm^{-1}) and $\text{NH}_3\text{-L}$ (1194 and 1594 cm^{-1}) began to appear on the surface [28], and due to their continuous accumulation, the peak intensity gradually increased. This indeed indicates that the nitrate species adsorbed on the MnO_x catalyst surface could react with adsorbed ammonia species, thereby following the Langmuir-Hinshelwood (L-H) mechanism. However, for $\text{Mn}_{0.90}\text{Mo}_{0.09}\text{V}_{0.01}\text{O}_x$ catalyst (Fig. 7H), the bands of monodentate nitrate (1554 cm^{-1}) and NO_2 (1610 cm^{-1}) species hardly changed within 1–5 min after introducing NH_3 , thereafter the two bands suddenly vanished in 10 min because of the accumulation and cover of surface ammonia species. Nonetheless, the infrared characteristic peak attributed to monodentate nitrate (1278 cm^{-1}) remained consistently detectable, albeit with a wavenumber shift from 1278 to 1290 cm^{-1} . This suggests that the nitrate species adsorbed on the $\text{Mn}_{0.90}\text{Mo}_{0.09}\text{V}_{0.01}\text{O}_x$ catalyst hardly reacted with the surface ammonia species at 100°C , indicating that the reaction followed the E-R mechanism.

For $\text{NH}_3\text{-SCR}$ reaction, catalytic mechanisms may differ between low and high-temperature ranges. Activity comparisons have revealed that incorporating of Mo and V into MnO_x significantly enhances catalytic

performance at medium-high temperatures. Consequently, conducting in situ DRIFTS tests at higher temperatures is imperative. The transient reactions between pre-adsorbed NH_3 and $\text{NO} + \text{O}_2$ as well as $\text{NO} + \text{O}_2$ adsorption at 220°C were investigated for MnO_x and $\text{Mn}_{0.90}\text{Mo}_{0.09}\text{V}_{0.01}\text{O}_x$ catalysts, respectively. As illustrated in Fig. 8A, after 15 min of NH_3 adsorption, two obvious bands related to $\text{NH}_3\text{-L}$ (1193 cm^{-1}) and coordinated NH_3 species (1302 cm^{-1}) appeared on the surface of pure MnO_x [60,61], and the intensity of the bands slowly enhanced with treatment time. After purging with N_2 for 30 min, the above two peaks have shifted to 1208 and 1314 cm^{-1} , respectively. As for the $\text{Mn}_{0.90}\text{Mo}_{0.09}\text{V}_{0.01}\text{O}_x$ catalyst (Fig. 8B), it was found that both the $\text{NH}_3\text{-L}$ (1203 cm^{-1}) [41] and $\text{NH}_4^+\text{-B}$ (1421 cm^{-1}) [22] could be observed after NH_3 adsorption in 15 min, moreover, the band intensity quickly increased with the extension of treatment time. After purging with N_2 for 30 min, the band at 1203 cm^{-1} shifted to 1211 cm^{-1} . It is worth noting that in comparison to MnO_x , the $\text{Mn}_{0.90}\text{Mo}_{0.09}\text{V}_{0.01}\text{O}_x$ catalyst not only possesses Lewis acid sites but also exhibits newly formed Brønsted acid sites, which is consistent with similar observations made at 100°C .

The reaction between the pre-adsorbed NH_3 species and the $\text{NO} + \text{O}_2$ mixed gases was also studied at 220°C . Firstly, the sample was pre-adsorbed NH_3 species for 50 min and then purged with N_2 for 30 min before introducing the $\text{NO} + \text{O}_2$ mixed gases. For MnO_x catalyst, as depicted in Fig. 8C, upon the introduction of $\text{NO} + \text{O}_2$, these bands corresponding to adsorbed ammonia species gradually diminished in intensity and completely disappeared within 15 min. The observation suggests that the coordinated NH_3 and $\text{NH}_3\text{-L}$ species participated in the SCR reaction. However, with the extension of reaction gas time for $\text{NO} + \text{O}_2$ introduction, no particularly evident infrared characteristic peaks related to N-containing species were observed, this indicates that gaseous NO has a relatively low tendency to adsorb onto the surface of MnO_x catalyst that pre-treated with NH_3 at 220°C . Similar experimental phenomena were observed on the $\text{Mn}_{0.90}\text{Mo}_{0.09}\text{V}_{0.01}\text{O}_x$ catalyst, as displayed in Fig. 8D, upon $\text{NO} + \text{O}_2$ introduction, the intensities of characteristic peaks related to $\text{NH}_4^+\text{-B}$ and $\text{NH}_3\text{-L}$ gradually diminished and disappeared entirely in 15 min. This signifies the participation and consumption of $\text{NH}_4^+\text{-B}$ and $\text{NH}_3\text{-L}$ species on the catalyst surface during the reaction. With prolonged reaction time, subsequent each data plot nearly formed a straight line, with no detectable characteristic peaks associated with N-containing species. This implies that NO did not adsorb onto the catalyst surface, revealing the adherence to a typical E-R mechanism, where gaseous NO reacted directly with adsorbed ammonia species.

Meanwhile, the adsorption behavior of NO on the catalysts at 220°C was also studied. As shown in Fig. S23, upon introducing NO , a faint peak related to monodentate nitrate (1347 cm^{-1}) [64] was detected on the surface of the MnO_x catalyst after 20 min. Subsequently, its peak intensity gradually increased with time. However, after purging with N_2 for 30 min, the characteristic peak disappeared completely from the catalyst surface. This indicates that NO can indeed adsorb on the surface of MnO_x , but with a weak adsorption strength. Therefore, the catalytic reaction also follows the L-H mechanism to some extent, but primarily adheres to the E-R mechanism at 220°C . In contrast, for the $\text{Mn}_{0.90}\text{Mo}_{0.09}\text{V}_{0.01}\text{O}_x$ catalyst (Fig. S24), with the introduction of $\text{NO} + \text{O}_2$, no characteristic peaks associated with N-containing species were detected throughout the entire 50-minute duration. Each subsequent data plot is nearly a straight line, suggesting that NO is very difficult to adsorb onto the surface. It is commonly believed that N_2O formation from the decomposition of NH_4NO_3 [1]. Furthermore, other researches have indicated that the primary factors influencing N_2O generation are [65]: (1) the thermal stability of NH_4NO_3 on the catalyst, and (2) the reduced catalytic activity of this catalyst in NO oxidation and subsequent surface nitrate formation, which likely contributes to higher SCR selectivity and less N_2O formation. The latter factor is considered the primary cause, as surface nitrates are the origin of NH_4NO_3 formation on the catalysts. In this study, we observed a lower NO -to- NO_2 conversion (Fig. 3C) and almost no surface nitrate formation on the

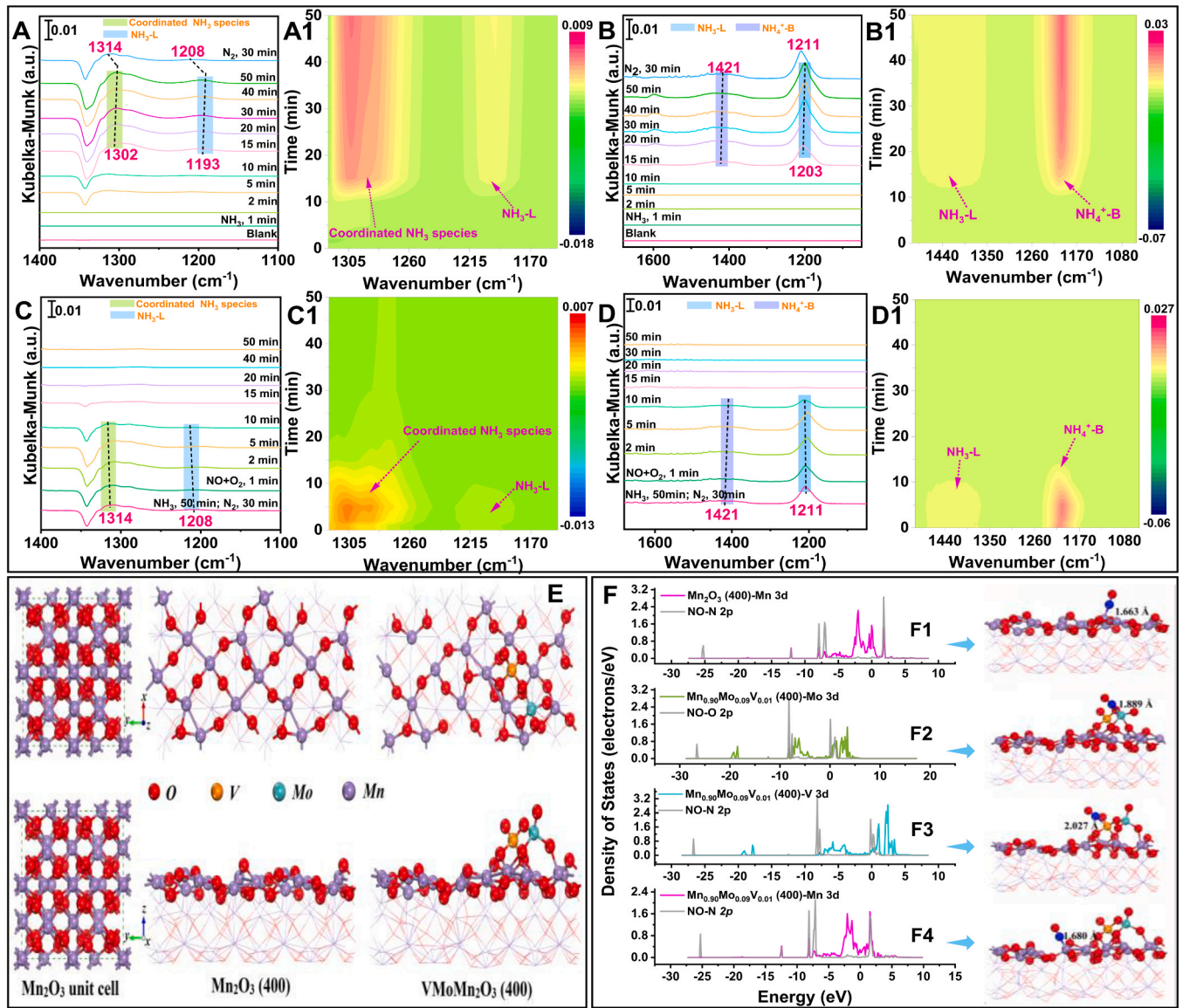
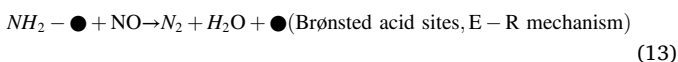
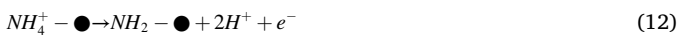
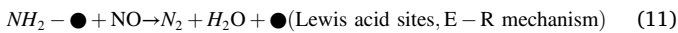
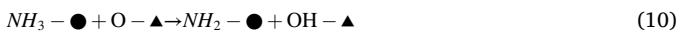


Fig. 8. In situ DRIFT spectra of NH₃ adsorption over (A, A1) MnO_x and (B, B1) Mn_{0.90}Mo_{0.09}V_{0.01}O_x catalysts at 220 °C. In situ DRIFT spectra for the reaction between pre-adsorbed NH₃ with NO + O₂ over (C, C1) MnO_x and (D, D1) catalysts at 220 °C. (E) Top view and side view of Mn₂O₃ unit cell and optimized multi-active center catalyst structure. (F) Optimized adsorption configurations and projected density of states (PDOS) of NO gas molecules on the multi-active center catalyst surface structure.

Mn_{0.90}Mo_{0.09}V_{0.01}O_x catalyst (Fig. 8D, Fig. S24), which could account for its boosted N₂ selectivity. The NH₃-SCR reaction on Mn_{0.90}Mo_{0.09}V_{0.01}O_x strictly follows the E-R mechanism. Based on both in situ DRIFTS results and previous research findings, it can infer that the reaction pathways on Mn_{0.90}Mo_{0.09}V_{0.01}O_x may proceed as follows: (● and ▲ represent surface active sites) [20]:



In summary, the in situ DRIFTS results above vividly demonstrate that the regulation of MnO_x with Mo and V, resulting in an increased number of Lewis acid sites and the emergence of new Brønsted acid sites. This, in turn, enhances the adsorption of NH₃. The catalytic reaction on the MnO_x catalyst mainly follows the L-H mechanism, but after regulation on the MnO_x, NH₃-SCR reaction only proceeds according to the E-R mechanism. Furthermore, the modulation by Mo and V accelerates the reaction between surface ammonia species and gaseous NO. These factors collectively contribute significantly to the improved catalytic performance of the Mn_{0.90}Mo_{0.09}V_{0.01}O_x catalyst.

To better understand how Mo and V regulation affects the NO adsorption capacity of MnO_x, we conducted DFT calculations using a Mn₂O₃ (400) surface model. This choice was made because Mn₂O₃ is the primary crystalline phase in the catalysts, and the (400) surface represents the most stable termination of manganese sesquioxide [66]. Based on relevant previous researches [67], the designed Mn₂O₃ unit cell and optimized multi-active center catalyst structure are illustrated in Fig. 8 (E). The optimized adsorption configurations and projected density of

states (PDOS) of NO gas molecules on the multi-active center catalyst surface structure are shown in Fig. 8 (F). The corresponding adsorption energy (E_{ads}) and newly formed bond information are summarized in Table S7. It is evident that NO can readily bind to the Mn center, signifying a strong chemical interaction as evidenced by the hybridization between N 2p and Mn 3d orbitals (Fig. 8F1). The N – Mn bond length measures 1.663 Å, and the observed adsorption energy stands at – 6.638 eV. As for the adsorption of the NO molecule on the $Mn_{0.90}Mo_{0.09}V_{0.01}O_x$ catalyst (Fig. 8F2), an increased E_{ads} of – 5.885 eV and an elongated bond length of 1.680 Å are observed, indicating that the Mn active centers in the catalyst are less prone to NO adsorption. Besides, as depicted in Fig. 8 (F3, F4), Mo or V active sites exhibit even weaker NO adsorption. Both the adsorption energy and resulting bond length notably increase, signifying weak physical adsorption of NO exclusively on Mo or V active sites. To sum up the DFT results, it is revealed that NO can readily adsorb onto Mn active sites in MnO_x . However, on the regulated $Mn_{0.90}Mo_{0.09}V_{0.01}O_x$, Mn active centers exhibit diminished NO adsorption. Notably, Mo and V active centers demonstrate minimal NO adsorption. These DFT findings align with the previously discussed in situ DRIFTS results, affirming that the dual regulation of Mo and V on MnO_x effectively hinders NO adsorption and shifts the catalytic mechanism towards the E-R mechanism for the catalytic reaction.

4. Conclusions

In this study, a series of highly active ternary $Mn_{0.90}Mo_{\delta}V_{0.10-\delta}O_x$ ($\delta = 0.01, 0.03, 0.05, 0.07, 0.09$) composite metal oxide catalysts were synthesized by simultaneously tuning the acidic and redox sites of MnO_x using Mo and V. $Mn_{0.90}Mo_{0.09}V_{0.01}O_x$ exhibited the highest catalytic activity and the strongest resistance to alkali metal poisoning. Analysis revealed that this dual-active sites regulation strategy significantly enhances the NH_3 -SCR activity by appropriately weakening the oxidation performance and increasing the quantity and strength of surface acid sites. Briefly, the regulation of Mo and V on MnO_x can transform some Mn_2O_3 into Mn_3O_4 with weaker oxidation performance, and Mn can also combine with Mo and V to form stable $MnMoO_4$ or $Mn-O-V$ species, which together properly weaken the oxidation performance of the catalyst. Moreover, the regulation of Mo and V on MnO_x can increase the medium-strong acid sites of the catalyst, which is beneficial for the adsorption of NH_3 at high temperatures. Both oxidative ability and acid sites strength of the catalyst do not follow a "stronger is better" trend. When these two factors are harmoniously balanced, the catalyst demonstrates the best NH_3 -SCR activity. In situ DRIFTS combined with DFT calculations indicate that after Mo and V tuned MnO_x , not only can the number of Lewis acid sites be increased, but also new Brønsted acid sites can be formed. The regulated catalyst can significantly inhibit the adsorption of NO and facilitate the catalytic reaction to proceed solely through the E-R mechanism, which could account for its enhanced N_2 selectivity. Alkali metals primarily affect catalysis by inhibiting oxidation capacity and reducing surface acidity. $Mn_{0.90}Mo_{0.09}V_{0.01}O_x$ maintains high catalytic activity post-alkali metal exposure due to optimal acid site preservation and oxidation capacity. The dual-active sites regulation strategy guides the preparation of high-performance NH_3 -SCR catalysts with robust alkali metal resistance.

CRediT authorship contribution statement

Li Zhenguo: Investigation, Methodology. **Zhang Hongxiang:** Investigation, Methodology. **Lu Shengyong:** Investigation, Methodology. **Zou Yu:** Investigation, Methodology. **Liu Wenming:** Methodology, Resources. **Li Yonglong:** Data curation, Formal analysis, Methodology, Visualization, Writing – original draft, Writing – review & editing. **Li Guobo:** Methodology, Resources. **Zhang Shule:** Investigation, Methodology. **Peng Honggen:** Funding acquisition, Project administration, Supervision, Writing – review & editing.

Declaration of Competing Interest

The authors declare that they have no known competing financial interests or personal relationships that could have appeared to influence the work reported in this paper.

Data Availability

Data will be made available on request.

Acknowledgments

This work was supported by the National Natural Science Foundation of China (22276076, 21976078 and 22306086), the Natural Science Foundation of Jiangxi Province (20202ACB213001, 20232BAB213029 and 20232BAB213028), the National Engineering Laboratory for Mobile Source Emission Control Technology (NELMS2019A12), the State Key Laboratory of Clean Energy Utilization (ZJUCEU2022015), and the Chongqing Natural Science Foundation (CSTB2023NSCQ-MSX0950), all of which are greatly acknowledged by the authors.

Appendix A. Supporting information

Supplementary data associated with this article can be found in the online version at doi:10.1016/j.apcatb.2023.123612.

References

- [1] L. Han, S. Cai, M. Gao, J. Hasegawa, P. Wang, J. Zhang, L. Shi, D. Zhang, Selective catalytic reduction of NO_x with NH_3 by using novel catalysts: state of the art and future prospects, *Chem. Rev.* 119 (2019) 10916–10976.
- [2] W. Qu, X. Liu, J. Chen, Y. Dong, X. Tang, Y. Chen, Single-atom catalysts reveal the dinuclear characteristic of active sites in NO selective reduction with NH_3 , *Nat. Commun.* 11 (2020) 1532.
- [3] J. Liu, X. Shi, Y. Yu, M. Zhang, D. Liu, H. He, Excellent hydrocarbon tolerance of $CeO_2-WO_3-SnO_2$ oxide catalyst for the NH_3 -SCR of NO_x , *Appl. Catal., B* 324 (2023), 122283.
- [4] Z. Lian, J. Wei, W. Shan, Y. Yu, P.M. Radjenovic, H. Zhang, G. He, F. Liu, J. Li, Z. Tian, H. He, Adsorption-induced active vanadium species facilitate excellent performance in low-temperature catalytic NO_x abatement, *J. Am. Chem. Soc.* 143 (2021) 10454–10461.
- [5] D.W. Kwon, D.H. Kim, S. Lee, J. Kim, H.P. Ha, A dual catalytic strategy by the nature of the functionalization effect as well as active species on vanadium-based catalyst for enhanced low temperature SCR, *Appl. Catal., B* 289 (2021), 120032.
- [6] J. Liu, G. He, W. Shan, Y. Yu, Y. Huo, Y. Zhang, M. Wang, R. Yu, S. Liu, H. He, Introducing tin to develop ternary metal oxides with excellent hydrothermal stability for NH_3 selective catalytic reduction of NO, *Appl. Catal., B* 291 (2021), 120125.
- [7] H. Liu, C. Gao, J. Chen, J. Mi, S. Yang, D. Chen, W. Si, Y. Peng, C. Sun, J. Li, Optimized local geometry and electronic structure of MoO_3/CeO_2 catalyst by adding copper cations for boosted nitrogen oxide reduction performance, *Appl. Catal., B* 332 (2023), 122742.
- [8] C. Chen, Y. Wang, J. Li, F. Tian, W. Chen, C. Feng, Y. Pan, Y. Liu, In situ construction of heteroatom F-doped Mn_3O_4 spinel catalysts with robust activity and SO_2 resistance for NH_3 -SCR at low temperature, *Appl. Catal., B* 338 (2023), 123086.
- [9] I. Song, H. Lee, S.W. Jeon, I.A.M. Ibrahim, J. Kim, Y. Byun, D.J. Koh, J.W. Han, D. H. Kim, Simple physical mixing of zeolite prevents sulfur deactivation of vanadia catalysts for NO_x removal, *Nat. Commun.* 12 (2021) 901.
- [10] Y. Yu, W. Tan, D. An, X. Wang, A. Liu, W. Zou, C. Tang, C. Ge, Q. Tong, J. Sun, L. Dong, Insight into the SO_2 resistance mechanism on $\gamma-Fe_2O_3$ catalyst in NH_3 -SCR reaction: a collaborated experimental and DFT study, *Appl. Catal., B* 281 (2021), 119544.
- [11] R. Wang, Z. Hao, X. Huang, Y. Peng, G. Liu, Y. Xia, S. Zhan, In-situ formation of carbon-doped cerium-zirconium solid solution as a superacid catalyst for the removal of NO_x , *Appl. Catal., B* 339 (2023), 123098.
- [12] D. Wang, Q. Chen, X. Zhang, C. Gao, B. Wang, X. Huang, Y. Peng, J. Li, C. Lu, J. Crittenden, Multipollutant control (MPC) of flue gas from stationary sources using SCR technology: a critical review, *Environ. Sci. Technol.* 55 (2021) 2743–2766.
- [13] H. Liu, F. Gao, S. Ko, N. Luo, X. Tang, H. Yi, Y. Zhou, Synthesis process and efficient NH_3 -SCR performance of alkali/alkaline earth metal-rich *Chlorella@Mn* catalyst, *Appl. Catal., B* 330 (2023), 122651.
- [14] Y. Wang, L. Chen, W. Wang, X. Wang, B. Li, S. Zhang, W. Li, S. Li, Revealing the excellent low-temperature activity of the $Fe_{1-x}Ce_xO_{3-5}$ catalyst for NH_3 -SCR: improvement of the lattice oxygen mobility, *ACS Appl. Mater. Interfaces* 15 (2023) 17834–17847.

- [15] C. Tang, H. Zhang, L. Dong, Ceria-based catalysts for low-temperature selective catalytic reduction of NO with NH₃, *Catal. Sci. Technol.* 6 (2016) 1248–1264.
- [16] S. Ma, X. Zhao, Y. Li, T. Zhang, F. Yuan, X. Niu, Y. Zhu, Effect of W on the acidity and redox performance of the Cu_{0.02}Fe_{0.2}W/TiO_x (a = 0.01, 0.02, 0.03) catalysts for NH₃-SCR of NO, *Appl. Catal., B* 248 (2019) 226–238.
- [17] W. Si, H. Liu, T. Yan, H. Wang, C. Fan, S. Xiong, Z. Zhao, Y. Peng, J. Chen, J. Li, Sn-doped rutile TiO₂ for vanadyl catalysts: Improvements on activity and stability in SCR reaction, *Appl. Catal., B* 269 (2020), 118797.
- [18] S. Ali, L. Chen, Z. Li, T. Zhang, R. Li, S.U.H. Bakhtiar, X. Leng, F. Yuan, X. Niu, Y. Zhu, Cu_xNb_{1-x} (x = 0.45, 0.35, 0.25, 0.15) bimetal oxides catalysts for the low temperature selective catalytic reduction of NO with NH₃, *Appl. Catal., B* 236 (2018) 25–35.
- [19] H. Wang, P. Ning, Y. Zhang, Y. Ma, J. Wang, L. Wang, Q. Zhang, Highly efficient WO₃-FeO_x catalysts synthesized using a novel solvent-free method for NH₃-SCR, *J. Hazard. Mater.* 388 (2020), 121812.
- [20] C. Gao, B. Xiao, J. Shi, C. He, B. Wang, D. Ma, Y. Cheng, C. Niu, Comprehensive understanding the promoting effect of Dy-doping on MnFeO_x nanowires for the low-temperature NH₃-SCR of NO_x: an experimental and theoretical study, *J. Catal.* 380 (2019) 55–67.
- [21] G. He, M. Gao, Y. Peng, Y. Yu, W. Shan, H. He, Superior oxidative dehydrogenation performance toward NH₃ determines the excellent low-temperature NH₃-SCR activity of mn-based catalysts, *Environ. Sci. Technol.* 55 (2021) 6995–7003.
- [22] N. Zhang, L. Li, Y. Guo, J. He, R. Wu, L. Song, G. Zhang, J. Zhao, D. Wang, H. He, A MnO₂-based catalyst with H₂O resistance for NH₃-SCR: Study of catalytic activity and reactants-H₂O competitive adsorption, *Appl. Catal., B* 270 (2020), 118860.
- [23] S. Chen, M.A. Vasiliades, Q. Yan, G. Yang, X. Du, C. Zhang, Y. Li, T. Zhu, Q. Wang, A.M. Efsthathiou, Remarkable N₂-selectivity enhancement of practical NH₃-SCR over Co_{0.5}Mn₁Fe_{0.25}Al_{0.75}O_x-LDO: the role of Co investigated by transient kinetic and DFT mechanistic studies, *Appl. Catal., B* 277 (2020), 119186.
- [24] M. Gao, Z. Li, G. He, Y. Shan, Y. Sun, H. He, Unveiling the origin of selectivity in the selective catalytic reduction of NO with NH₃ over oxide catalysts, *Environ. Sci. Technol.* 57 (2023) 8426–8434.
- [25] M. Li, M. Gao, G. He, Y. Yu, H. He, Mechanistic insight into the promotion of the low-temperature NH₃-selective catalytic reduction activity over Mn_xCe_{1-x}O_y catalysts: a combined experimental and density functional theory study, *Environ. Sci. Technol.* 57 (2023) 3875–3882.
- [26] L. Li, J. Ji, W. Tan, W. Song, X. Wang, X. Wei, K. Guo, W. Zhang, C. Tang, L. Dong, Enhancing low-temperature NH₃-SCR performance of Fe–Mn/CeO₂ catalyst by Al₂O₃ modification, *J. Rare Earths* 40 (2022) 1454–1461.
- [27] G. Xu, X. Guo, X. Cheng, J. Yu, B. Fang, A review of Mn-based catalysts for low-temperature NH₃-SCR: NO_x removal and H₂O/SO₂ resistance, *Nanoscale* 13 (2021) 752–778.
- [28] X. Yao, L. Chen, J. Cao, Y. Chen, M. Tian, F. Yang, J. Sun, C. Tang, L. Dong, Enhancing the deNO_x performance of MnO_x/CeO₂-ZrO₂ nanorod catalyst for low-temperature NH₃-SCR by TiO₂ modification, *Chem. Eng. J.* 369 (2019) 46–56.
- [29] Y. Geng, W. Shan, S. Yang, F. Liu, W-modified Mn–Ti mixed oxide catalyst for the selective catalytic reduction of NO with NH₃, *Ind. Eng. Chem. Res.* 57 (2018) 9112–9119.
- [30] W. Liao, X. Fang, B. Cen, J. Chen, Y. Liu, M. Luo, J. Lu, Deep oxidation of propane over WO₃-promoted Pt/BN catalysts: the critical role of Pt–WO₃ interface, *Appl. Catal., B* 272 (2020), 118858.
- [31] H. Wang, M. Lin, T. Murayama, S. Feng, M. Haruta, H. Miura, T. Shishido, Ag size/structure-dependent effect on low-temperature selective catalytic oxidation of NH₃ over Ag/MnO₂, *ACS Catal.* 11 (2021) 8576–8584.
- [32] S.T. Oyama, X. Zhang, J. Lu, Y. Gu, T. Fujitani, Epoxidation of propylene with H₂ and O₂ in the explosive regime in a packed-bed catalytic membrane reactor, *J. Catal.* 257 (2008) 1–4.
- [33] W. Kohn, L.J. Sham, Self-consistent equations including exchange and correlation effects, *Phys. Rev.* 140 (1965) A1133.
- [34] B. Hammer, L.B. Hansen, J.K. Nørskov, Improved adsorption energetics within density-functional theory using revised Perdew–Burke–Ernzerhof functionals, *Phys. Rev. B* 59 (1999) 7413.
- [35] J.P. Perdew, K. Burke, M. Ernzerhof, Generalized gradient approximation made simple, *Phys. Rev. Lett.* 77 (1996) 3865.
- [36] S.L. Dudarev, G.A. Botton, S.Y. Savrasov, C.J. Humphreys, A.P. Sutton, Electron-energy-loss spectra and the structural stability of nickel oxide: an LSDA+ U study, *Phys. Rev. B* 57 (1998) 1505.
- [37] J.C. Avila-Gaxiola, J.G. Ibarra-Armenta, R.E. Félix-Medina, S. Meza-Aguilar, C. Demangeat, A magnetic map of O/Fe/Mn/Fe (001) multilayer with DFT+ U scheme, *Surf. Sci.* 718 (2022), 122006.
- [38] M. García-Mota, A. Vojvodic, F. Abild-Pedersen, J.K. Nørskov, Electronic origin of the surface reactivity of transition-metal-doped TiO₂ (110), *J. Phys. Chem. C* 117 (1) (2013) 460–465.
- [39] Z. Jia, Y. Shen, T. Yan, H. Li, J. Deng, J. Fang, D. Zhang, Efficient NO_x abatement over alkali-resistant catalysts via constructing durable dimeric VO_x species, *Environ. Sci. Technol.* 56 (4) (2022) 2647–2655.
- [40] L. Li, P. Li, W. Tan, K. Ma, W. Zou, C. Tang, L. Dong, Enhanced low-temperature NH₃-SCR performance of CeTiO_x catalyst via surface Mo modification, *Chin. J. Catal.* 41 (2020) 364–373.
- [41] Z. Liu, S. Zhang, J. Li, L. Ma, Promoting effect of MoO₃ on the NO_x reduction by NH₃ over CeO₂/TiO₂ catalyst studied with in situ DRIFTS, *Appl. Catal., B* 144 (2014) 90–95.
- [42] C. Liu, J. Shi, C. Gao, C. Niu, Manganese oxide-based catalysts for low-temperature selective catalytic reduction of NO_x with NH₃: A review, *Appl. Catal. A* 522 (2016) 54–69.
- [43] D. Meng, W. Zhan, Y. Guo, Y. Guo, L. Wang, G. Lu, A highly effective catalyst of Sm–MnO_x for the NH₃-SCR of NO_x at low temperature: promotional role of sm and its catalytic performance, *ACS Catal.* 5 (2015) 5973–5983.
- [44] W. Ren, D. Liu, C. Sun, X. Yao, J. Tan, C. Wang, K. Zhao, X. Wang, Q. Li, L. Mai, Nonhierarchical heterostructured Fe₂O₃/Mn₂O₃ porous hollow spheres for enhanced lithium storage, *Small* 14 (2018) 1800659.
- [45] B. Li, J. Shen, H. Zhao, W. Lei, X. Yu, J. Xu, Y. Tang, H. Zhang, H. Shao, In-situ formed amorphous manganese vanadate encapsulating MnO via salt-assisted ball milling toward 3D hierarchical porous electrodes for superior lithium storage, *Chem. Eng. J.* 431 (2022), 133732.
- [46] L. Mai, F. Yang, Y. Zhao, X. Xu, L. Xu, Y. Luo, Hierarchical MnMoO₄/CoMoO₄ heterostructured nanowires with enhanced supercapacitor performance, *Nat. Commun.* 2 (2011) 381.
- [47] J. Yesuraj, V. Elumalai, M. Bhagavathiachari, A.S. Samuel, E. Elaiyappillai, P. M. Johnson, A facile sonochemical assisted synthesis of α-MnMoO₄/PANI nanocomposite electrode for supercapacitor applications, *J. Electroanal. Chem.* 797 (2017) 78–88.
- [48] F. Kapteijn, L. Singoredjo, A. Andreini, J.A. Moulijn, Activity and selectivity of pure manganese oxides in the selective catalytic reduction of nitric oxide with ammonia, *Appl. Catal., B* 3 (1994) 173–189.
- [49] F. Yu, X. Xu, H. Peng, H. Yu, Y. Dai, W. Liu, J. Ying, Q. Sun, X. Wang, Porous NiO nano-sheet as an active and stable catalyst for CH₄ deep oxidation, *Appl. Catal. A* 507 (2015) 109–118.
- [50] Y. Xin, H. Li, N. Zhang, Q. Li, Z. Zhang, X. Cao, P. Hu, L. Zheng, J.A. Anderson, Molecular-Level Insight into Selective Catalytic Reduction of NO_x with NH₃ to N₂ over a Highly Efficient Bifunctional V_a-MnO_x Catalyst at Low Temperature, *ACS Catal.* 8 (2018) 4937–4949.
- [51] W. Yang, Y. Peng, Y. Wang, Y. Wang, H. Liu, Z.A. Su, W. Yang, J. Chen, W. Si, J. Li, Controllable redox-induced in-situ growth of MnO₂ over Mn₂O₃ for toluene oxidation: active heterostructure interfaces, *Appl. Catal., B* 278 (2020), 119279.
- [52] J. Mu, X. Li, W. Sun, S. Fan, X. Wang, L. Wang, M. Qin, G. Gan, Z. Yin, D. Zhang, Inductive effect boosting catalytic performance of advanced Fe_{1-x}V_xO₈ catalysts in low-temperature NH₃ selective catalytic reduction: insight into the structure, interaction, and mechanisms, *ACS Catal.* 8 (2018) 6760–6774.
- [53] Z. Chen, Q. Yang, H. Li, X. Li, L. Wang, S. Chi Tsang, Cr–MnO_x mixed-oxide catalysts for selective catalytic reduction of NO_x with NH₃ at low temperature, *J. Catal.* 276 (2010) 56–65.
- [54] R. Wang, Z. Hao, Y. Li, G. Liu, H. Zhang, H. Wang, Y. Xia, S. Zhan, Relationship between structure and performance of a novel highly dispersed MnO_x on Co–Al layered double oxide for low temperature NH₃-SCR, *Appl. Catal., B* 258 (2019), 117983.
- [55] C. Sun, H. Liu, W. Chen, D. Chen, S. Yu, A. Liu, L. Dong, S. Feng, Insights into the Sm/Zr co-doping effects on N₂ selectivity and SO₂ resistance of a MnO_x-TiO₂ catalyst for the NH₃-SCR reaction, *Chem. Eng. J.* 347 (2018) 27–40.
- [56] L. Li, L. Zhang, K. Ma, W. Zou, Y. Cao, Y. Xiong, C. Tang, L. Dong, Ultra-low loading of copper modified TiO₂/CeO₂ catalysts for low-temperature selective catalytic reduction of NO by NH₃, *Appl. Catal., B* 207 (2017) 366–375.
- [57] F. Liu, W. Shan, Z. Lian, J. Liu, H. He, The smart surface modification of Fe₂O₃ by WO_x for significantly promoting the selective catalytic reduction of NO with NH₃, *Appl. Catal., B* 230 (2018) 165–176.
- [58] R. Wu, L. Li, N. Zhang, J. He, L. Song, G. Zhang, Z. Zhang, H. He, Enhancement of low-temperature NH₃-SCR catalytic activity and H₂O & SO₂ resistance over commercial V₂O₅-MoO₃/TiO₂ catalyst by high shear-induced doping of expanded graphite, *Catal. Today* 376 (2021) 302–310.
- [59] X. Xia, W. Lei, Q. Hao, W. Wang, X. Wang, One-step synthesis of CoMoO₄/graphene composites with enhanced electrochemical properties for supercapacitors, *Electrochim. Acta* 99 (2013) 253–261.
- [60] X. Li, J. Li, Y. Peng, H. Chang, T. Zhang, S. Zhao, W. Si, J. Hao, Mechanism of arsenic poisoning on SCR catalyst of CeW/Ti and its novel efficient regeneration method with hydrogen, *Appl. Catal., B* 184 (2016) 246–257.
- [61] Z. Fan, J. Shi, C. Gao, G. Gao, B. Wang, C. Niu, Rationally designed porous MnO_x-FeO_x nanoneedles for low-temperature selective catalytic reduction of NO_x by NH₃, *ACS Appl. Mater. Interfaces* 9 (2017) 16117–16127.
- [62] L. Chen, F. Yuan, Z. Li, X. Niu, Y. Zhu, Synergistic effect between the redox property and acidity on enhancing the low temperature NH₃-SCR activity for NO removal over the Co_{0.2}Ce_xMn_{0.8-x}Ti₁₀ (x = 0–0.40) oxides catalysts, *Chem. Eng. J.* 354 (2018) 393–406.
- [63] L. Yan, Y. Ji, P. Wang, C. Feng, L. Han, H. Li, T. Yan, L. Shi, D. Zhang, Alkali and phosphorus resistant zeolite-like catalysts for NO_x reduction by NH₃, *Environ. Sci. Technol.* 54 (2020) 9132–9141.
- [64] L. Yan, Y. Gu, L. Han, P. Wang, H. Li, T. Yan, S. Kuboon, L. Shi, D. Zhang, Dual promotional effects of TiO₂-decorated acid-treated MnO_x octahedral molecular sieve catalysts for alkali-resistant reduction of NO_x, *ACS Appl. Mater. Interfaces* 11 (2019) 11507–11517.
- [65] H. Chen, Z. Wei, M. Kollar, F. Gao, Y. Wang, J. Szanyi, C.H.F. Peden, A comparative study of N₂O formation during the selective catalytic reduction of NO_x with NH₃ on zeolite supported Cu catalysts, *J. Catal.* 329 (2015) 490–498.
- [66] Y. Xin, L. Cheng, Y. Lv, J. Jia, D. Han, N. Zhang, J. Wang, Z. Zhang, X. Cao, Experimental and theoretical insight into the facet-dependent mechanisms of NO oxidation catalyzed by structurally diverse Mn₂O₃ nanocrystals, *ACS Catal.* 12 (2022) 397–410.
- [67] X. Yu, M. Shi, Y. Fan, L. Yang, J. Zhang, W. Liu, W. Dai, S. Zhang, L. Zhou, X. Luo, S. Luo, Activation or passivation: influence of halogen dopant (F, Cl, Br) on photochemical activity of Mn₂O₃ in degrading toluene, *Appl. Catal., B* 309 (2022), 121236.